

# Large eddy simulation of breaking waves

Erik Damgaard Christensen\*, Rolf Deigaard

*Department of Hydrodynamics and Water Resources (ISVA), Building 115, Technical University of Denmark, DK-2800 Lyngby, Denmark*

Received 2 September 1999; received in revised form 26 May 2000; accepted 29 May 2000

---

## Abstract

A numerical model is used to simulate wave breaking, the large scale water motions and turbulence induced by the breaking process. The model consists of a free surface model using the surface markers method combined with a three-dimensional model that solves the flow equations. The turbulence is described by large eddy simulation where the larger turbulent features are simulated by solving the flow equations, and the small scale turbulence that is not resolved by the flow model is represented by a sub-grid model. A simple Smagorinsky sub-grid model has been used for the present simulations. The incoming waves are specified by a flux boundary condition. The waves are approaching in the shore-normal direction and are breaking on a plane, constant slope beach. The first few wave periods are simulated by a two-dimensional model in the vertical plane normal to the beach line. The model describes the steepening and the overturning of the wave. At a given instant, the model domain is extended to three dimensions, and the two-dimensional flow field develops spontaneously three-dimensional flow features with turbulent eddies. After a few wave periods, stationary (periodic) conditions are achieved. The surface is still specified to be uniform in the transverse (alongshore) direction, and it is only the flow field that is three-dimensional.

The turbulent structures are investigated under different breaker types, spilling, weak plungers and strong plungers. The model is able to reproduce complicated flow phenomena such as obliquely descending eddies. The turbulent kinetic energy is found by averaging over the transverse direction. In spilling breakers, the turbulence is generated in a series of eddies in the shear layer under the surface roller. After the passage of the roller the turbulence spreads downwards. In the strong plunging breaker, the turbulence originates to a large degree from the topologically generated vorticity. The turbulence generated at the plunge point is almost immediately distributed over the entire water depth by large organised vortices. Away from the bed, the length scale of the turbulence (the characteristic size of the eddies resolved by the model) is similar in the horizontal and the vertical direction. It is found to be of the order one half of the water depth. © 2001 Elsevier Science B.V. All rights reserved.

*Keywords:* Surf zone; Breaking waves; Plunging breaker; Turbulence; Numerical model; Large eddy simulation

---

## 1. Introduction

The wave breaking in a surf zone generates rotational flows over a large range of scales, from vortices with dimensions comparable to the water depth, surface rollers at the fronts of spilling breakers or

---

\* Corresponding author. Present address: DHI Water and Environment, Artens Allé 11, DK-2970 Hørsholm, Denmark.  
*E-mail address:* edc@dhi.dk (E.D. Christensen).

broken waves with a scale comparable to the wave height to the turbulence with eddies down to a size of fractions of a millimetre. Energy is transferred from the motion of one scale to another. The waves lose energy which is transferred to large scale water motions in the breaking process. The large almost two-dimensional vortices break up into three-dimensional flow structures and generate the large scale turbulent motion. The energy moves through the cascade process from the smaller to the larger wave numbers in the turbulence spectrum, to be dissipated to heat by the viscous forces.

In this study, plunging and spilling breakers are considered. A plunging breaker starts by the wave front turning over and projecting forward as a tongue of water or a jet, which then falls down at the trough in front of the crest. A spilling breaker may be seen to start as a very weak plunging breaker at the crest of the wave, the rotational flow generated by the plunger then spreads down along the front of the wave developing into a surface roller. It can be difficult to make an exact distinction between the two regimes. The details of the flow field in breaking waves are of importance for understanding many processes in the surf zone. One example is the distribution of the driving forces due to the wave breaking, which is entering the force balance for the wave set-up and for the wave-driven currents in the surf zone. Another example is the vertical and horizontal exchange of momentum and suspended sediment, which determines the velocity distribution of the longshore current and the undertow and the sediment concentration field.

The turbulent flow field has been the subject of intensive experimental studies. Most investigations have been carried out in the laboratory, where the well controlled conditions make a systematic study possible, but field measurements have also been made of turbulence in breaking waves, e.g. George et al. (1994). Among the most important experimental investigations are: Stive (1980), Nadaoka and Kondoh (1982), Jansen (1986), Nadaoka et al. (1988), Nadaoka et al. (1989), Okayasu et al. (1988), Lin and Hwung (1992) and Ting and Kirby (1994, 1995, 1996).

The investigations of Ting and Kirby have demonstrated many of the differences between the turbulence in spilling and plunging breakers. In a

spilling breaker much of the turbulence is dissipated in the upper part of the water column, close to the location of production of turbulence under the surface roller. In a plunging breaker the turbulence is initially associated with large vortices that rapidly spread the turbulence over the vertical so that the turbulence saturates the whole water column. The intensity of the turbulence under the plunger is much higher under the wavefront, and it decays very much from the passage of one wave to the next. This is in contrast to spilling breakers, where the intensity of the turbulence at a given level may not decay considerably between each passage of a wavefront.

There is a considerable interest in the flow field generated by the jet or tongue of water hitting the water surface in front of the wave crest. Jansen (1986) investigated the flow field in the upper part of the waves in both spilling and plunging breakers by tracing particles. Lin and Hwung (1992) studied the velocity field in weak plunging breakers with a similar technique. In both studies it was found that in plunging breakers the jet of water is almost totally reflected when it hits the water surface. In this initial phase of the breaking a system of eddies is formed with opposite direction of rotation. The jet re-splashes several times and generates a series of horizontal eddies. Basco (1985) found in contrast the plunger to penetrate the surface. After the penetration a roller was developed in front of the wave without any re-splash. The different behaviour of the jet is related to the strength of the plunger, cf. Peregrine (1983). For weak and moderate plunging waves, the rebounding jet is most common, while an extreme plunger on a very steep beach may be more likely to penetrate the surface. Battjes (1988) has pointed out that the overturning of the wave generates topological induced vorticity as the cross-section of the wave changes from being a singly connected area to being a doubly connected area at the instant when the jet hits the surface. The topologically induced vorticity can be strong, but initially the motion is well ordered with a low turbulence intensity.

Nadaoka et al. (1988, 1989) used visualization techniques and LDA to study the three-dimensional structure of the vortices in breaking waves. They found that the horizontal vortices formed in the breaking process are deformed and break up into what is described as obliquely descending eddies.

The obliquely descending eddies have their axes approximately in the vertical plane normal to the wave crest, with a slope so that the upper end is furthest in the propagation direction. It has been argued that these oblique eddies can be expected to be of significance for the exchange of momentum and sediment and for the entrainment of air bubbles under breaking waves.

Theoretical models for breaker induced flow fields have included qualitative descriptions based on laboratory experiments (Basco, 1985) and relations for the level of turbulent kinetic energy and the turbulence length scale under spilling breakers and broken waves based on measured quantities and a budget for the turbulent kinetic energy (Svendsen, 1987). By use of a simple one-equation turbulence model, Deigaard et al. (1986) attempted to describe the time variation of the turbulent kinetic energy over a vertical in a surf zone in order to model the vertical exchange of suspended sediment and of momentum. In the model of Deigaard et al. (1986), the rate of production of turbulence due to the breaking was estimated from the wave parameters and introduced as a source term in the turbulence model. The simple one-equation turbulence model has been combined with a Boussinesq wave model for surf zone conditions (Schäffer et al., 1993, Madsen et al., 1997a, 1997b) to obtain a phase resolving cross-shore sediment transport model, Rakha et al. (1997). Sakai et al. (1986) has studied the vortex formation and the splash down of the jet in a plunging breaker by a two-dimensional (vertical and cross-shore) hydrodynamic model with a free surface condition described by the Marker and Cell (MAC) method. By coupling a two-dimensional hydrodynamic model with a free surface condition and a turbulence model (two-equation,  $k$ -epsilon) the energy loss in the hydrodynamic model is simulated and fed directly into the turbulence model as done by Lemos (1992) and in later extensive studies by Lin and Liu (1998a,b), who has been able to simulate a number of characteristic features of spilling and plunging breakers. Pedersen et al. (1995) used a discrete vortex model to simulate the large vortices generated by a plunging breaker. The model included bed boundary layer model and was used to describe the intense stirring up of suspended sediment under plunging breakers. Zhao and Tanimoto (1998) applied the Large Eddy Simulation

(LES) method in two-dimensional flow simulations with a description of the free surface based on the volume of fluid method. They used the model to describe vertical flow patterns in breaking waves. Three-dimensional LES with a free surface has been used to simulate the turbulent flow field and the water surface around a surface-piercing cylinder (Mayer et al., 1998; Kawamura et al., 2000).

The present study concerns numerical simulation of the water motion in breaking waves. The simulations are all with a constant slope beach and normally incident regular waves. The simulations are with a free surface and different types of breakers are considered. The hydrodynamic model is three-dimensional and it resolves the larger structures of the turbulence generated by the wave breaking using LES. This simulation technique has been chosen in order to describe the transformation of the initially two-dimensional horizontal vortices generated by the breaking into three-dimensional structures and turbulence. While the internal flow structures are modelled by a three-dimensional flow model the water surface is only two-dimensional. It is assumed to be uniform in the alongshore direction.

## 2. The numerical model

The numerical model consists of a number of elements which are combined with a formulation of the boundary conditions for simulation of breaking waves. The main elements are: (i) a solver for the Navier–Stokes equations, (ii) a subgrid scale model for the turbulence that is not resolved in the grid used for the solution of the Navier–Stokes equations and (iii) a model for the free surface. The models are based on existing theory and methods, and are therefore only outlined briefly.

### 2.1. The Navier–Stokes solver

The Navier–Stokes equation can be written in tensor notation as follows:

$$\frac{\partial u_i}{\partial t} + \frac{\partial u_i u_j}{\partial x_j} = -\frac{1}{\rho} \frac{\partial p}{\partial x_i} + \frac{\partial}{\partial x_j} \left( \nu_e \left( \frac{\partial u_i}{\partial x_j} + \frac{\partial u_j}{\partial x_i} \right) \right) \quad (1)$$

where  $u_i$  is the flow velocity vector:  $u_i = (u, v, w)$ ,  $t$  is time,  $x_i$  is the space coordinate:  $x_i = (x, y, z)$ ,  $\rho$  is the density of water,  $p$  is the pressure and  $\nu_e$  is the viscosity. The viscosity  $\nu_e$  can be interpreted as the kinematic viscosity  $\nu$  of the water in the case of direct numerical simulations or as the sum of the kinematic viscosity and an eddy viscosity  $\nu_t$  for simulations based on a turbulence model or a subgrid scale model. The continuity equation reads:

$$\frac{\partial u_i}{\partial x_i} = 0 \quad (2)$$

The equations are discretized on a rectangular domain with rectangular grid cells and they are integrated over a grid cell, conserving momentum, cf. Ferziger and Peric (1999). This is the basis of the finite volume method, which in the present case with a rectangular grid and only one computational node per cell is equivalent to a finite difference method in conservative form. Details of the numerical scheme are found in Christensen (1998), and only a brief outline of the model is given. The flow equations are solved on a rectangular staggered grid. A single computational cell (centred at the position:  $x_i = (i\Delta x_1, j\Delta x_2, k\Delta x_3)$ , where  $\Delta x_1$ ,  $\Delta x_2$  and  $\Delta x_3$  are the grid sizes in the three dimensions) is illustrated

in Fig. 1, where the defined relative position of the three velocity components and the pressure can be seen. As an example, the momentum equation in the  $x_1$ -direction (determining the velocity component  $u_{i,j,k}$  at the next time step) is formulated as an integral over the dotted cell in Fig. 1 whereby the pressure acts directly on the two faces of the cell in the  $x_2$ – $x_3$  plane.

The solution is made by an explicit scheme following the SOLA-VOF procedure described by Nichols et al. (1980). The main steps are:

- From a given time step  $n$ , a predicted velocity field for the next time step is found from the momentum Eq. (1) without any pressure gradients:

$$u_i^{(n+1)*} = (\text{CONV}^n + \text{DIFF}^n)\Delta t + u^n \quad (3)$$

where  $u_i^{(n+1)*}$  is the predicted velocity for time step  $n + 1$ , CONV and DIFF are the convective and the diffusive terms in the flow equations (last term on the left and right hand side of Eq. (1), respectively),  $\Delta t$  is the time step and  $u^n$  is the velocity field at time step  $n$ .

- The predicted velocity field is not required to fulfill the continuity equation, and the deviation  $D$

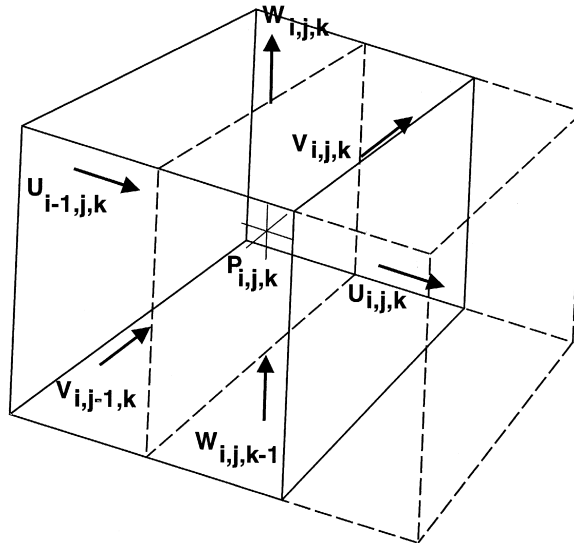


Fig. 1. A single cell of the computational grid: velocities are defined on the surface of the cell, other variables (e.g. the pressure) are defined at the centre of the cell.

from the equation of conservation of mass is found as the divergence of the predicted velocity field:

$$D = \frac{\partial u_i^{(n+1)*}}{\partial x_i} \quad (4)$$

- The difference between the corrected velocity field and the predicted velocity field is due to the effect of the pressure in the flow equation, and the corrected velocities are found as:

$$u_i^{n+1} = u_i^{(n+1)*} - \frac{1}{\rho} \frac{\partial p^{n+1}}{\partial x_i} \Delta t \quad (5)$$

- The pressure in Eq. (5) is found by taking the divergence at each side of the equation. The divergence of the left hand side must be zero due to the continuity equation, and the pressure at time step  $(n+1)$  is determined from the Poisson equation with  $D$  in the ‘source’ term:

$$\frac{\partial^2 p^{n+1}}{\partial x_i^2} = \frac{\rho}{\Delta t} D \quad (6)$$

- The corrected velocity field is found by correcting the predicted velocity field with the pressure field, according to Eq. (5).

When determining the predictor velocity  $u_i^{(n+1)*}$  the momentum terms have been determined by use of the QUICKEST scheme (Leonard, 1979). This third order upwind scheme is derived for one dimension, but it is often used in two- or three-dimensional models, see e.g. Mason and Callen (1986).

The solution of the Poisson Eq. (6) is very time consuming, using about half of the total CPU time used for a simulation. The Successive Over-Relaxation (SOR) method and the Preconditioned Conjugate Gradient method have both been used for the present study.

The module for solving the Navier–Stokes equations have been verified by two simulations: a driven cavity flow and a direct simulation of a turbulent channel flow, as described in Appendix A.

## 2.2. The subgrid scale model

At high Reynolds’ numbers, it is not realistic to resolve all the turbulent fluctuations in a numerical computation. The concept of LES has therefore been

introduced to represent the effect of the small scale turbulence, which is not resolved by the model, on the large scale turbulent fluctuations, which are represented directly in the calculated velocity and pressure field.

The basis for the LES simulation is a spatial filtering of the Navier–Stokes’ equation (Leonard, 1974). For finite difference or finite volume methods, a top-hat filter is simple to apply and is often used. The width of the filter depends on the grid size, which means that for a finer grid a larger part of the turbulent motion is represented directly in the simulation. This is in contrast to conventional turbulence models (e.g. the k-epsilon model) where the flow equations are averaged in time, and only the mean velocity field is obtained from the model regardless of how fine the grid is made.

The filtered flow equations read:

$$\begin{aligned} \frac{\partial \bar{u}_i}{\partial t} + \frac{\partial \bar{u}_i \bar{u}_j}{\partial x_j} = & -\frac{1}{\rho} \frac{\partial \bar{p}}{\partial x_i} + \nu \frac{\partial^2 \bar{u}_i}{\partial x_j^2} \\ & - \frac{\partial}{\partial x_j} (\overline{u_i u_j} - \bar{u}_i \bar{u}_j) \end{aligned} \quad (7)$$

$$\frac{\partial \bar{u}_i}{\partial x_i} = 0 \quad (8)$$

where an overbar signifies a filtered quantity. In Eq. (7), the last term on the right hand side has to be modelled in order to obtain a closure. Different more or less sophisticated procedures have been developed for this closure, where the term is split up into several terms that are modelled separately or where the term is modelled as a whole (see Germano et al. (1991), Germano (1992) or Chapter 2 in Galperin and Orszag (1993)). For the present simulations, the Smagorinsky (1963) closure has been applied. It is a simple and robust closure model, and probably the LES closure that has been applied for the greatest variety of flow situations, and for which most experience has been gained. It has therefore been chosen for these first simulations of three-dimensional turbulence in a surf zone. The more sophisticated models have been developed, e.g. to obtain simulations that are more independent of the grid size than the Smagorinsky based models. The advanced closure models have been developed and calibrated to be

used for example for a hydraulically smooth bed with at least a partial resolution of the viscous sublayer and will typically require a resolution that cannot be obtained in the present simulations.

In the Smagorinsky model, the last term on the right hand side of Eq. (7) is modelled as a whole, by introducing an eddy viscosity to represent the momentum exchange by the sub grid scale turbulence. The eddy viscosity is determined from the strain rate in the flow field that is resolved by the model. In this way, the model works as a mixing length model on the subgrid scale level:

$$v_t = (C_s \Delta)^2 \sqrt{2\overline{S_{i,j}}\overline{S_{i,j}}} \quad (9)$$

where  $\overline{S_{i,j}}$  is the strain rate that can be written as:

$$\overline{S_{i,j}} = \frac{1}{2} \left( \frac{\partial \overline{u}_i}{\partial x_j} + \frac{\partial \overline{u}_j}{\partial x_i} \right) \quad (10)$$

and  $\Delta$  is a length scale dependent on the grid size:

$$\Delta = (\Delta x_1 \times \Delta x_2 \times \Delta x_3)^{1/3} \quad (11)$$

The parameter  $C_s$  is the Smagorinsky constant. It is empirical and has to be determined from comparisons between experiments and model simulations. The Smagorinsky model has been found to give a reasonable representation of homogeneous and isotropic turbulence. Applications of the Smagorinsky closure model have typically been made with values of the Smagorinsky constant from 0.1 to 0.2. The present simulations have used a value of 0.1.

In the case of a hydraulically smooth bed, a very fine resolution is required near the bed to resolve the conditions in the viscous sublayer, and to reduce the number of computational points the near bed conditions are often represented by wall functions. The use of wall functions is in any case necessary in the case of a hydraulically rough bed. For the present simulations, a very simple wall function has been used, which relates the velocity at the computational point closest to the bed to the instantaneous shear stress at the bed, where it has been assumed that the combination of the shear stress found from the sub-grid model and the viscous shear stress is dominant in the lowest computational points. A quadratic resistance law based on a logarithmic velocity profile is used to describe the relation between the instantane-

ous bed shear stress and the near bed flow velocity.

The LES model has been verified by simulating a channel flow, details of which are given in Appendix A.

### 2.3. The free surface model

The free surface is described by the Surface Marker and Cell method (SM-method). The method used is based on Chen et al. (1991, 1995). A large number of particles are positioned at the surface, and for each time step the particles are advected by the simulated velocity field. Each cell is categorized as being a surface cell (containing surface markers), a full cell or an empty cell. The status of each cell is checked and corrected at each time step. The position of the surface is estimated from the status of the cells and the amount of water in each surface cell, which is found on basis of the position of the surface markers. The boundary condition of a pressure equal to zero is then introduced at the surface in the Poisson equation determining the pressure field by using the irregular star technique as in Miyata (1986).

The SM-method does not ensure that the total volume of water in the computational domain is conserved. In order to optimize the conservation of water in the computational domain, a predictor–corrector procedure was applied (cf. Christensen, 1998), where the markers are moved at the beginning of the time step. The velocity field after the time step is found from the flow equations and the predicted positions of the markers, the corrected positions of the markers are then found from the new velocity field and the velocity field from the previous time step:

$$x_{i,\text{marker}}^{n+1} = x_{i,\text{marker}}^n + \Delta t (u_{i,\text{marker}}^{n+1} + u_{i,\text{marker}}^n) / 2 \quad (12)$$

where  $x_{i,\text{marker}}$  is the position of the marker and  $u_{i,\text{marker}}$  is the velocity vector at the marker position, interpolated from the velocities in the gridpoints. Initially, the surface markers are aligned on a string along the surface. The markers are numbered from one to the total number of markers. In the breaking process, the string of marker may fold over, and a

S	E	E	E	E	E	E	F
F	S	S	E	E	E	E	E
F	F	F	S	S	E	E	E
F	F	F	F	F	S	S	E
F	F	F	F	F	F	F	S

Fig. 2. Flagging of cells. Not all cells containing markers are flagged as surface cells.

large number of cells that are neighbours are to be surface cells. To avoid large areas of surface cells in the interior of the flow field, all surface cells that do not have an empty cell as neighbour are reflagged to be full cells, as illustrated in Fig. 2. Similarly, surface cells that do not have a full cell as neighbour are reflagged to be empty. When the surface folds over in the breaking process, many markers are covered by water; this does not create a problem immediately, but to reduce the number of unnecessary markers, all markers that are situated in a full cell without a surface cell as neighbour are eliminated. If the distance between the markers become too large, new markers are added to the string. It was found that to obtain a reasonable resolution of the surface, each surface cell must contain at least four markers per cell width. The overturning of the surface and the necessary reflagging of a large number of neighbouring cells from surface cells to full cells has the consequence that additional water is created in the model area at each breaking event.

The free surface model has been validated by two-dimensional simulations in the  $x$ - $z$  plane. Details of a dam break simulation and comparison with

measurements of the advancement of the toe of the front are given in Appendix A. As illustrated in Appendix A, the simulation with predictor–corrector method showed much less gain and loss of water than the simulation with the simpler one-step procedure for updating the marker positions.

The propagation of a solitary wave over a horizontal bed has been simulated in a  $320 \times 44$  cell domain. The length of the domain is 40 times the water depth. The wave height was 0.4 time the water depth and the initial condition has been taken from a third order solitary wave theory (cf. Fenton, 1972). The simulated propagation velocity is exact (within one per thousand), and when using sufficiently small time steps, the wave height is constant when propagating over a distance of 12 times the water depth. During this period of time, the net loss of water has been  $3 \cdot 10^{-4}$  of the total volume. The simple one-step procedure for updating the marker positions gave a loss of water more than two times larger than the predictor–corrector method.

Finally, the shoaling and breaking of a solitary wave on a constant slope (1 to 35) has been simulated. The breaking wave is a plunging breaker. Comparison has been made between model results and measurements by Grilli et al. (1994), who present measurements of the cross-shore variation in the wave height up to the point of wave breaking. The predicted shoaling up to the break-point is in good agreement with the measurements, Fig. 3. A stretch of 16 m of the sloping beach is represented by a total of 1200 computational cells along the slope and 80 cells normal to it. The grid size along the first 8 m is twice as large as along the last 8 m of the beach. The two-dimensional wave simulations are made with a specified viscosity of zero.

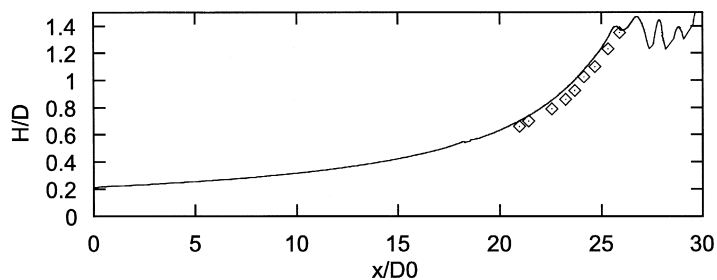


Fig. 3. The wave height of a shoaling and breaking solitary wave: bed slope: 1/35, depth at the boundary: 0.44 m, wave height at the boundary: 0.088 m. Points: measurements by Grilli et al. (1994).

### 3. The combined model

The different elements described above are combined into a model for breaking waves. The simulations are made for a plane, constant slope beach. The computational domain for the Navier–Stokes solver is a rectangular block. The beach is covered by a series of computational blocks (multi block system) placed side by side with the lower boundary coinciding with the bed, Fig. 4. The number of grid points in a given direction is the same for all blocks, and the grids are rectangular with constant grid size within a block. The ratio between the grid sizes of two neighbouring blocks have to be 1, 2 or 1/2. If the grid sizes are identical, the pressure and the velocity at the boundaries are simply copied from one grid to the other, otherwise interpolation is necessary. The simulation includes the shoaling process which takes place over a considerable distance outside the surf zone. The modelling of propagation and shoaling of the waves do not require as fine a resolution as modelling of the breaking process, and a coarser resolution is therefore used in the outer part of the model domain.

At the offshore boundary, the velocity field is prescribed on basis of a wave theory. Solitary wave theory or second order Stokes theory has been applied. The instantaneous distribution of the velocity profile is determined by the theory. The instantaneous position of the water surface at the boundary is a result of the simulation, and the absolute magnitude of the velocities at the boundary is determined so that the instantaneous flux of water, integrated from the bed to the surface, is identical to the flux predicted by the wave theory. By this procedure,

fluctuations of the water level at the boundary, causing fluctuations in the flux of water at the boundary, are prevented.

In a three-dimensional computational block, the position of the free surface is taken to be uniform in the  $y$ -direction (shore-parallel direction). This means that each surface marker can be interpreted as a line parallel with the  $y$ -axis. The markers are moved by the  $x$ - and  $z$ -components of the velocity field, averaged over the width of the domain. The surface velocities used in the three-dimensional flow calculation are found from the averaged velocity field. This acts as a numerical filter, which smooths out the velocities at the surface to some extent, while the use of the local surface velocities could cause instabilities and a blow-up of the simulation. The pressure in the surface cells is found in every  $x$ – $z$ -section as if this section was a two-dimensional model in its own. This means that the pressure is not necessarily constant in the longshore direction in the surface cells, especially since a high level of turbulence near the surface can cause variations in the pressure.

The first few wave periods are simulated by a purely two-dimensional model. At a given instant, the modelling domain in the surf zone is extended to three dimensions by adding extra sections in the longshore direction and using the two-dimensional velocity and pressure fields, the marker positions and the status of the cells (full, surface or empty) as a hot-start initial condition for the three-dimensional simulation. The velocity field spontaneously develops three-dimensional flow structures which rapidly grow and develop into fully turbulent structures generated by the wave breaking process. No initial perturbation is introduced and the three-dimensional

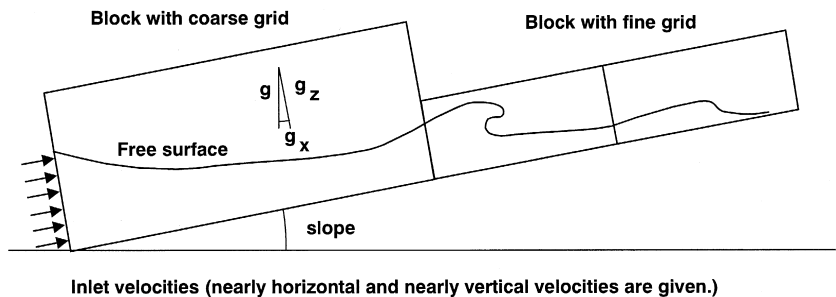


Fig. 4. An example of the computational grid for two-dimensional simulations composed of three blocks.

structures originate from minute cross-shore variations introduced in the solution of the flow equations.

#### 4. Breaker types in the simulations

The types of breakers obtained in the model are illustrated by a series of two-dimensional simulations. The three most important breaker types are spilling breakers, plunging breakers and surging breakers. The Surf Similarity Parameter,  $\xi_0$  (cf. Battjes, 1974), is the parameter that has been used most frequently to predict the breaker type in a given situation.  $\xi_0$  is defined as:

$$\xi_0 = \frac{\tan(\beta)}{\sqrt{H_0/L_0}} \quad (13)$$

where  $\beta$  is the beach slope,  $H_0$  is the deepwater wave height and  $L_0$  is the deep water wavelength. For small values of  $\xi_0$ , the breakers will be spilling and for increasing values, the breaker type is changing to plunging and surging. The key parameters for the three wave conditions that have been considered are given in Table 1.

Fig. 5 shows a spilling breaker, the beach slope is 1/20 and the surf similarity parameter has the value 0.30, which corresponds to a spilling breaker according to the analysis of Galvin (1968). The wave period is 1.4 s and the wave height at the boundary is 0.08 m at a water depth of 0.32 m. The wave shown is the fourth in the simulation, and the time between two frames in the sequence in Fig. 5 is one tenth of the wave period. It can be seen that a very small jet

shoots forward at the crest of the wave in the first frame, but it is almost immediately in contact with the surface in front of it and a shear layer and a surface roller is developing. From the shear layer, a number of eddies develops as the breaker propagates. The ratio between the wave height and water depth at breaking was 0.8, which is in good agreement with experimental results.

The surf similarity parameter for the situation illustrated in Fig. 6 is 0.44, which according to Galvin (1968) should be in the range for spilling breakers. However, with a beach slope of 1/13.5, the conditions are similar to the experiments by Lin and Hwung (1992), who classified the breakers as plunging. In the following, they will be referred to as weakly plunging breakers. The wave period and the incoming wave height are identical to the conditions for the spilling breaker case. In the initial stages of the breaking, a tongue of water is thrown forward in front of the crest, which gives the clear impression of a plunging breaker. The plunger does not penetrate when it falls down into the trough, but rebounds instead. A region of low momentum can be seen under the region of impingement, which is in agreement with the observations of Lin and Hwung (1992). The ratio of wave height to water depth at the break point is in the range 0.95 to 1.0, which is close to the value 0.99 found by Lin and Hwung (1992). It should be noted that the small ‘finger’ of water at the front of the broken wave in the last panel of Fig. 6 is unphysical and is caused by the relatively coarse resolution in the flow simulations.

The breaker in Fig. 7 is a strong plunger, with a surf similarity parameter of 0.56. The bed slope is 1/13.5, the wave period is 1.4 s and the incoming wave height is 0.05 m at the water depth 0.32 m. At

Table 1  
Parameters for the three wave conditions

Breaker type	Spilling	Weak plunger	Strong plunger
Bed slope, $\tan(\beta)$	1/20	1/13.5	1/13.5
Depth at boundary	0.321 m	0.321 m	0.321 m
Wave height at boundary	0.08 m	0.08 m	0.05 m
Wave period, $T$	1.4 s	1.4 s	1.4 s
Deep water steepness, $H_0/L_0$	0.0281	0.0281	0.0176
Surf similarity parameter, $\xi_0$	0.30	0.44	0.56
Breaker index, $H_b/D_b$	0.8	1.0	1.2

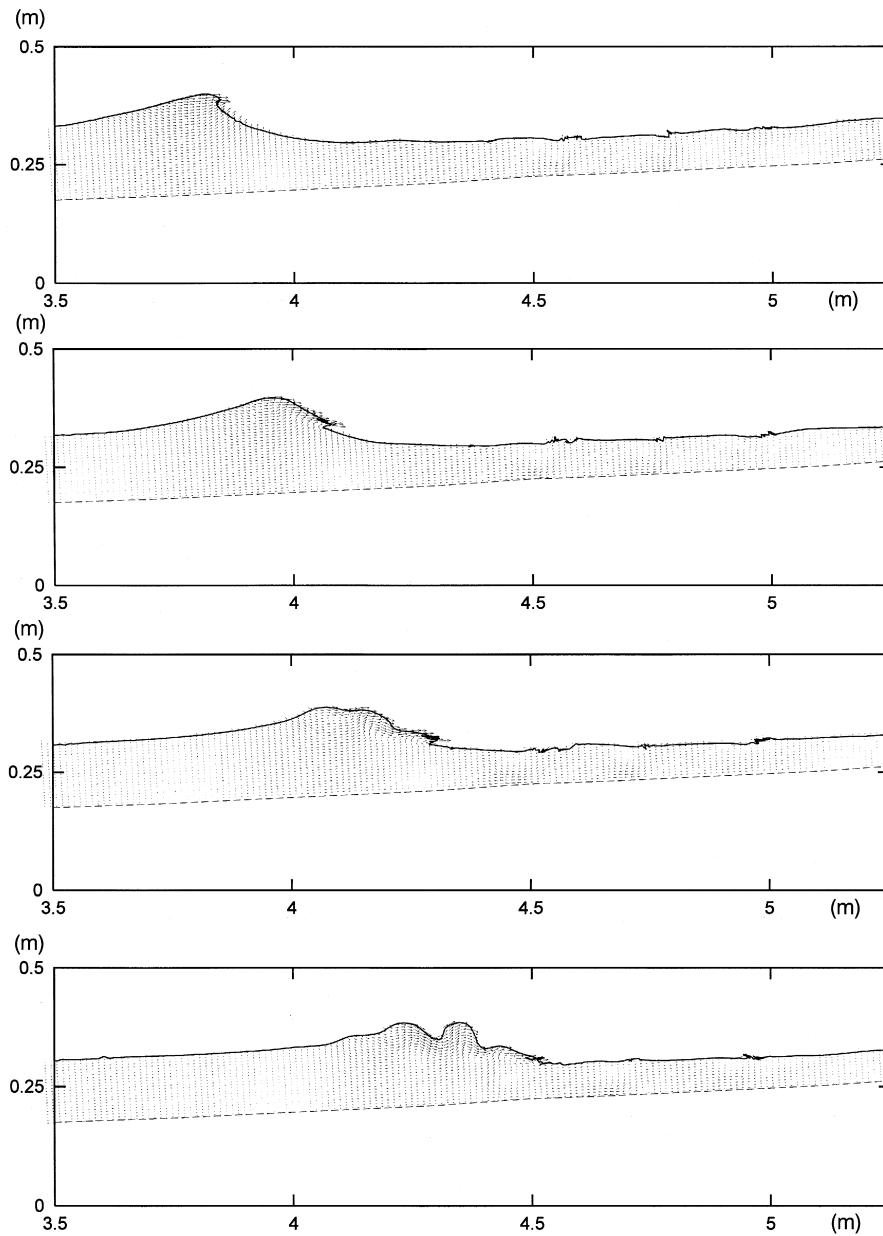


Fig. 5. The initial breaking of a spilling breaker, two-dimensional simulation. This is the fourth wave to break from the start of the simulation.

breaking, the ratio between the wave height and the water depth is between 1.1 and 1.2. The plunger rebounds when it hits the surface and pushes a mass of water up in front of it. The vorticity that is

induced topologically (cf. Battjes, 1988) when the plunger touches the trough in front of the crest is strong, and the eddy associated with it extends over most of the water depth, cf. panel 2 and 3 in Fig. 7.

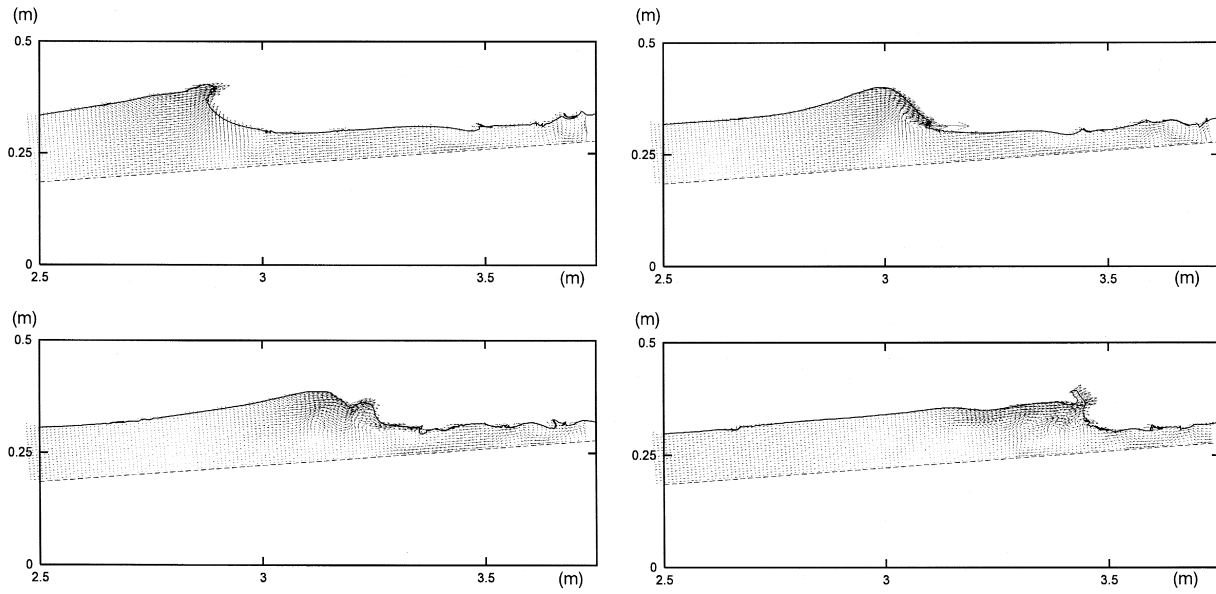


Fig. 6. The initial breaking of a weak plunging breaker, two-dimensional simulation. This is the fourth wave to break from the start of the simulation.

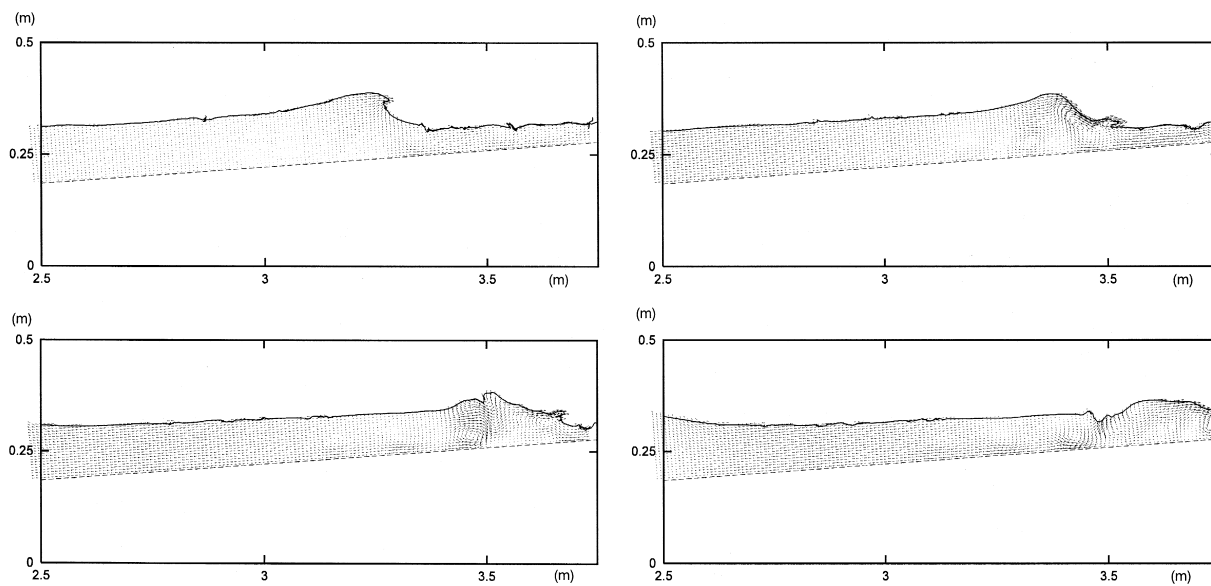


Fig. 7. The initial breaking of a strong plunging breaker, two-dimensional simulation. This is the fourth wave to break from the start of the simulation.

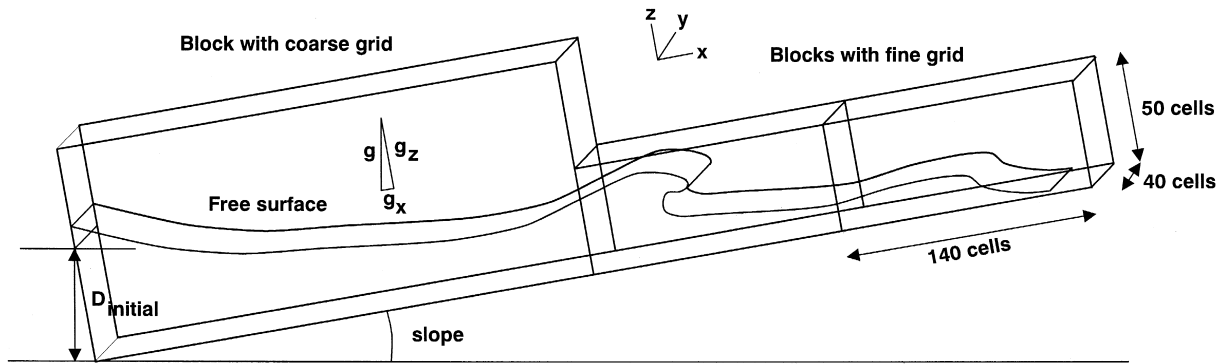


Fig. 8. An example of the computational domain for three-dimensional simulations composed of three blocks.

## 5. Three-dimensional simulations

### 5.1. Model set-up for the three-dimensional simulations

For the three-dimensional simulations, the number of grid points in each computational block is  $(N_x, N_y, N_z) = (140, 40, 50)$ . One large block is placed at the offshore end of the domain, it has the dimensions  $2.5 \text{ m} \times 0.3 \text{ m} \times 0.6 \text{ m}$ . A number of small blocks ( $1.25 \text{ m} \times 0.3 \text{ m} \times 0.3 \text{ m}$ ) is placed onshore of the large block, Fig. 8. For the cases of spilling and strong plunging breakers, three small blocks are used; for the case of weak plunging breakers, two small blocks are used. Typically, the simulation of one wave period consisting of 2800 time steps with three blocks required 6 h of CPU-time on a Cray vector-processor placed at the computer centre UNI-C in Lyngby.

### 5.2. The three-dimensional structure of the flow field

The structure of the velocity field generated by the three-dimensional simulations is analysed by considering plots of the velocities in a number of cross-sections. Fig. 9 shows the velocity field in the

$x$ - $z$  plan, the vorticity in the cross-section and the pressure field in a three-dimensional simulation of the weak plunger just after the wave has broken. The jet or tongue of water of the plunger hits the water surface almost where the horizontal wave induced velocities change sign from the onshore directed flow under the incoming wave to the offshore directed velocity field of the back-rush of the previous wave. The increased stagnation pressure under the impingement point is clear. A region of low momentum fluid is formed under the plunger, and the momentum of the plunging tongue is not sufficient to penetrate the surface, and it rebounds. Behind the plunge point, a region of high vorticity is formed during the initial breaking, which can be interpreted as topologically generated vorticity. The phenomena observed in Fig. 9 are very similar to the two-dimensional simulation with similar boundary conditions illustrated in Fig. 6.

The temporal development of the turbulence under the weak plunger in a fixed  $y$ - $z$  cross-section at  $x$  equals 3.21 m is shown in Fig. 10. The panels are separated by one tenth of a wave period. In the first panel, very little turbulence is present, in the two following turbulence from the previous breaker has been advected into the cross-section by the back-rush.

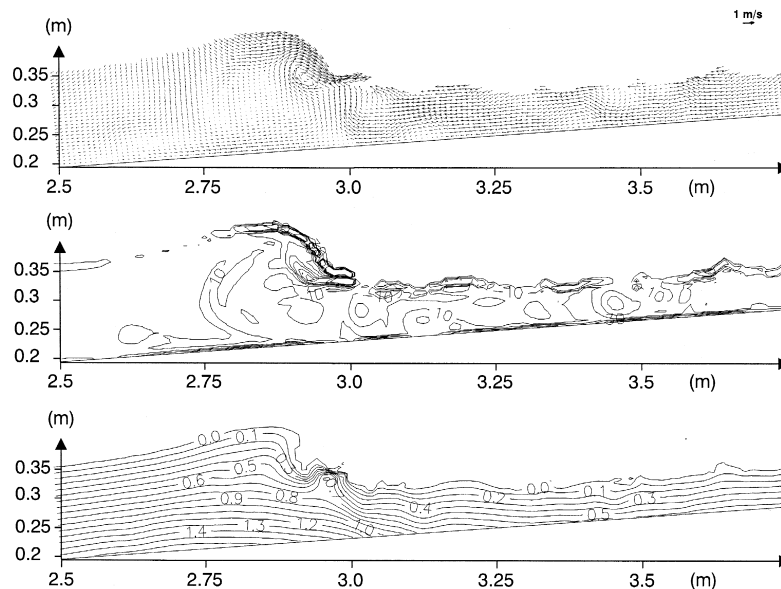


Fig. 9. An example of the flow field in a weak plunging breaker illustrated by a vector plot of the velocity field, a vorticity plot and a pressure plot.

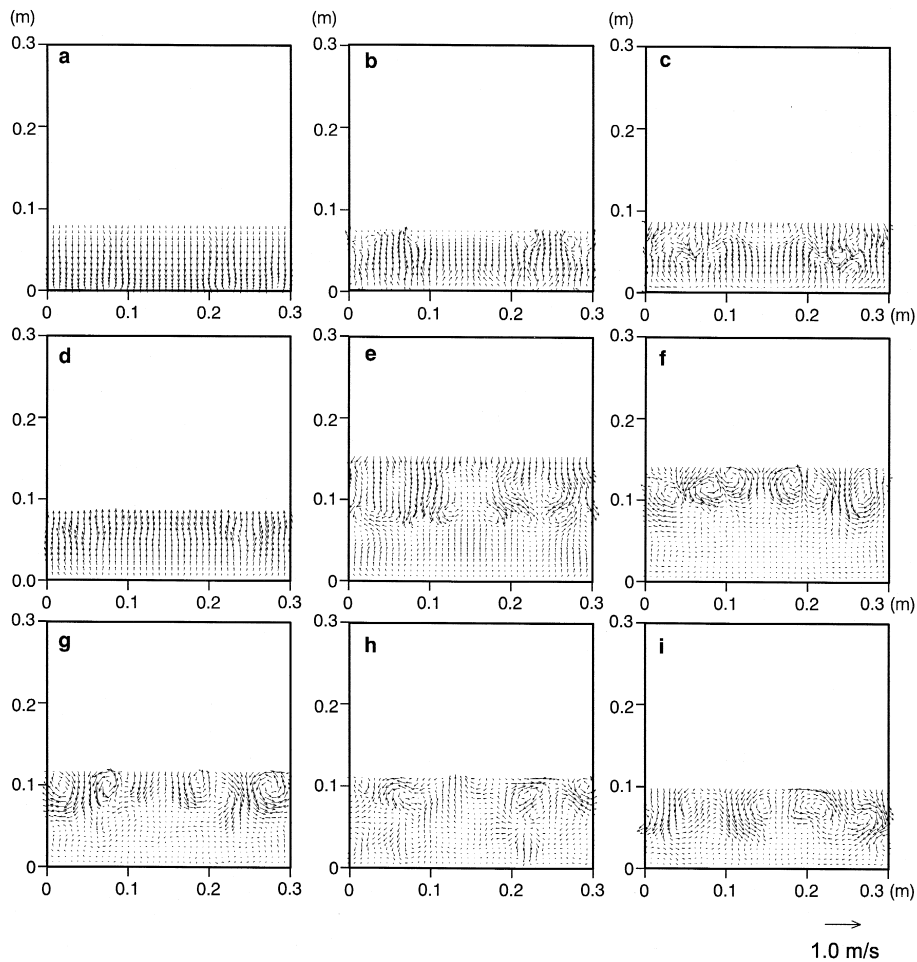


Fig. 10. A cross-section from a weak plunging breaker at  $x = 3.21$  m. The panels are separated by one tenth of a wave period.

The last five panels show how the turbulence is generated by the breaker when it reaches the cross-section and how the turbulence is spreading over the vertical. A typical scale of the turbulent eddies is about  $1/5$  of the width of the computational domain. The figure illustrates how the local variation in the turbulence can be affected by the cross-shore advection of turbulence.

An instantaneous three-dimensional flow field illustrating the turbulence generated by a passing breaking wave (weak plunger) can be seen in Fig. 11. Ten cross-sections and two longitudinal sections are shown. The positions of the cross-sections are indicated in the longitudinal sections. In some cases, an eddy structure can be identified from one cross-

section to the next, and in that case the position of the centres has been marked. A line through the centres shows the orientation of an eddy, and the pattern of obliquely descending eddies which was identified by Nadaoka et al. (1988, 1989), can clearly be recognised. The two longitudinal sections show the  $u-w$  velocity field at each side of the longest of the obliquely descending eddies, the positions of the centre-points are also indicated. The systematic differences in the velocity fields in the two longitudinal sections are clearly seen. In the following analysis of the turbulent kinetic energy, it is found that the obliquely descending eddies are located at local maximum in the intensity of the turbulence that has been left by the passing breaker. Obliquely descending

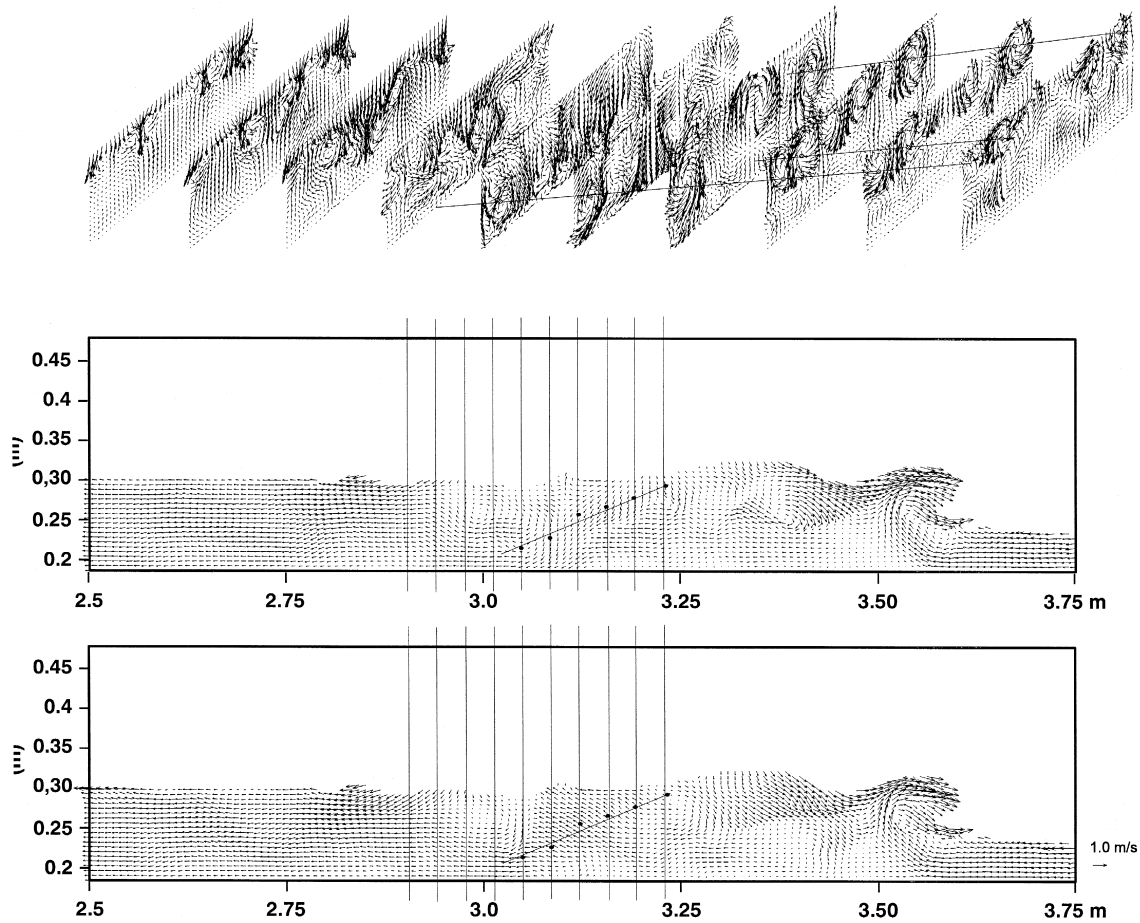


Fig. 11. An example of a velocity field with obliquely descending eddies in a weak plunging breaker.

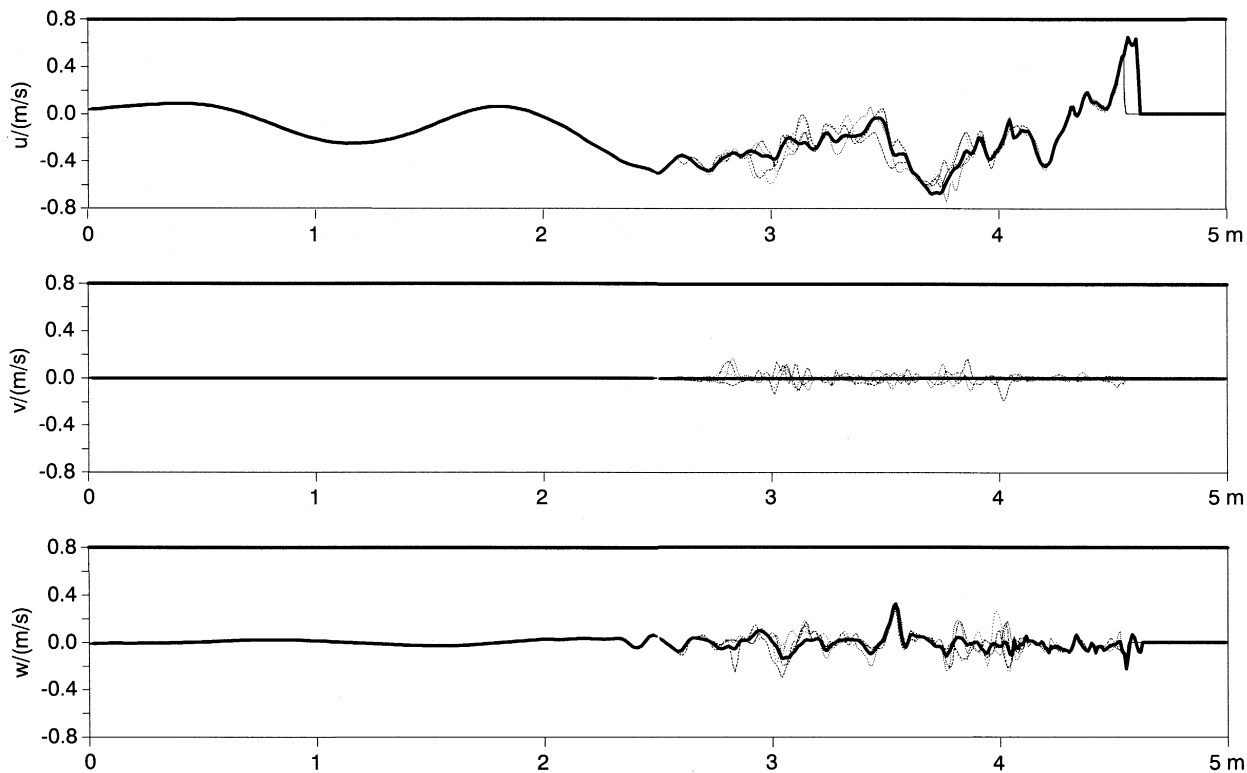


Fig. 12. The velocities in a section at a distance of 3.3 cm from the bed, weak plunger at the same instance as in Fig. 11. The thick line shows the velocities averaged over the transverse direction. The other curves show the velocities along three lines. Top:  $u$ -component, Middle:  $v$ -component, Bottom:  $w$ -component.

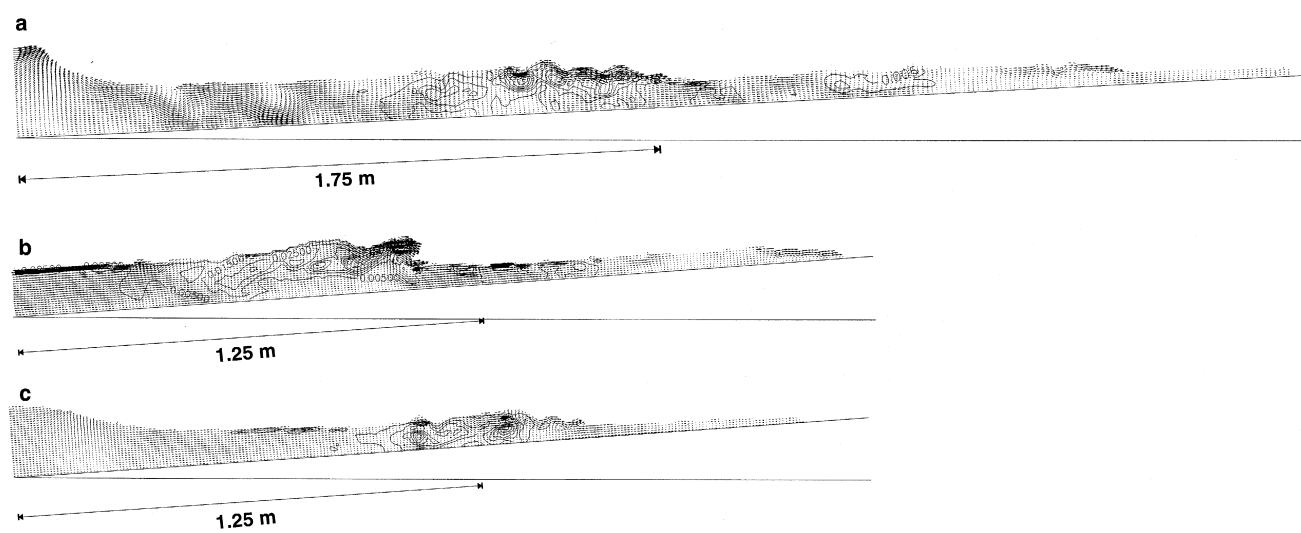


Fig. 13. Examples of the distribution of the turbulent kinetic energy in a spilling breaker, a weak plunging breaker and a strong plunging breaker. The contour lines for  $k$  [ $\text{m}^2/\text{s}^2$ ] are given for  $0.005 \text{ m}^2/\text{s}^2$ ,  $0.015 \text{ m}^2/\text{s}^2$ ,  $0.025 \text{ m}^2/\text{s}^2$ , etc.

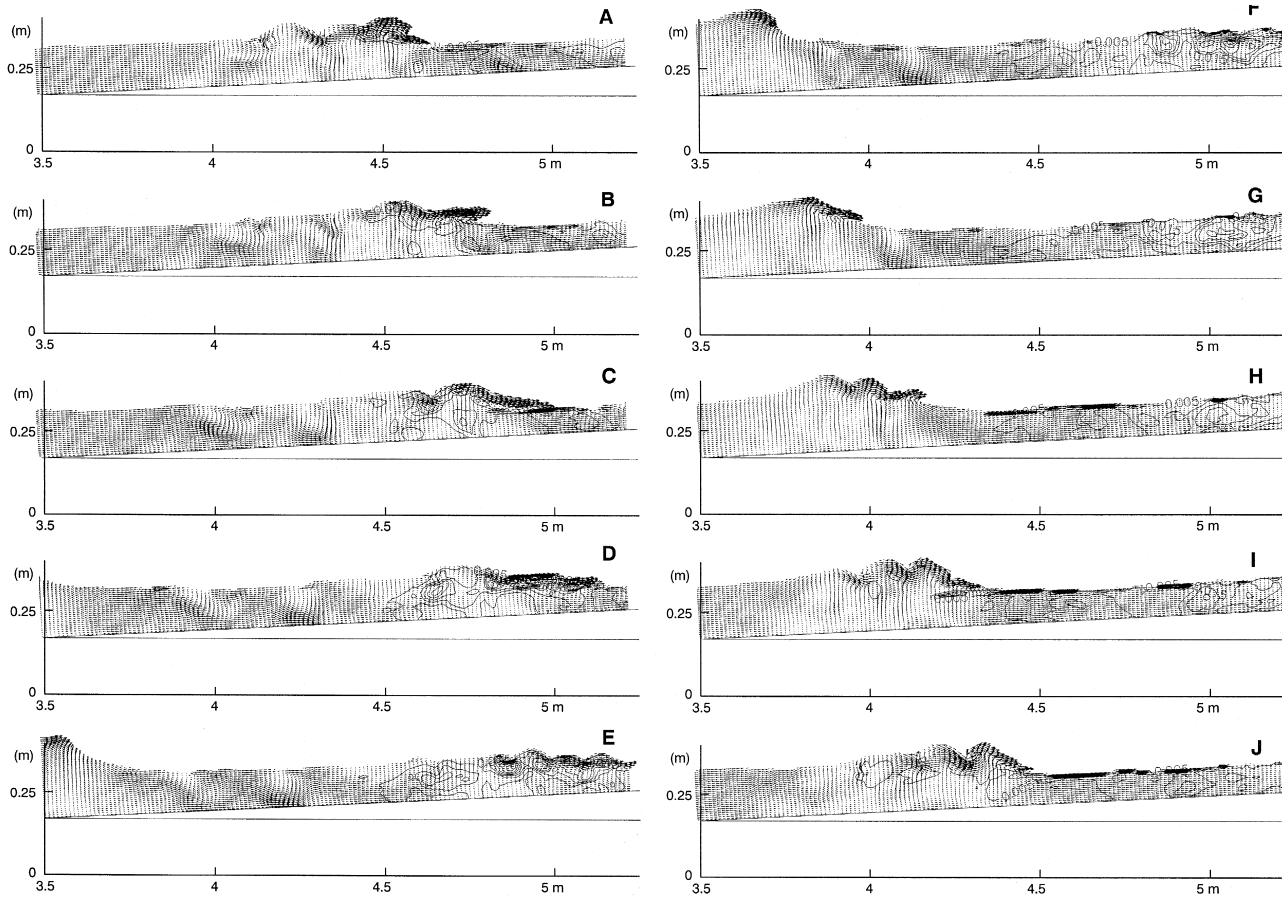


Fig. 14. The time evolution of the turbulent kinetic energy in a spilling breaker. Contour lines as in Fig. 13.

eddies were not found in all the simulations, sometimes longitudinal eddies with horizontal axes were observed instead.

### 5.3. Turbulent kinetic energy and length scales

Direct numerical simulations and large eddy simulations are in many respects similar to experimental investigations with respect to the problem of distinguishing between the turbulent fluctuations and the ordered water motion. In a steady flow, the mean velocity can be determined by time averaging and the turbulent fluctuations are then found as the difference between the actual velocity and the mean velocity. In time varying flow — and in wave motion in particular — the determination of the

turbulent velocity fluctuations is much more complicated, and no definite solution has yet been found. To determine the turbulence from measurements in a surf zone mainly two approaches have been applied: filtering and ensemble averaging. In the first, the time series are filtered to distinguish between the high frequency fluctuations, defined as turbulence, and the signal in the low frequency band, which is defined as the ordered motion. In order to be successful, the time scales of the turbulence must be much smaller than the wave period. This is not always the case, and especially at the passage of a front of a breaking or broken wave it can be very difficult to determine which part of a time varying signal that is turbulence and which part that is part of the ordered wave induced motion. Ensemble averag-

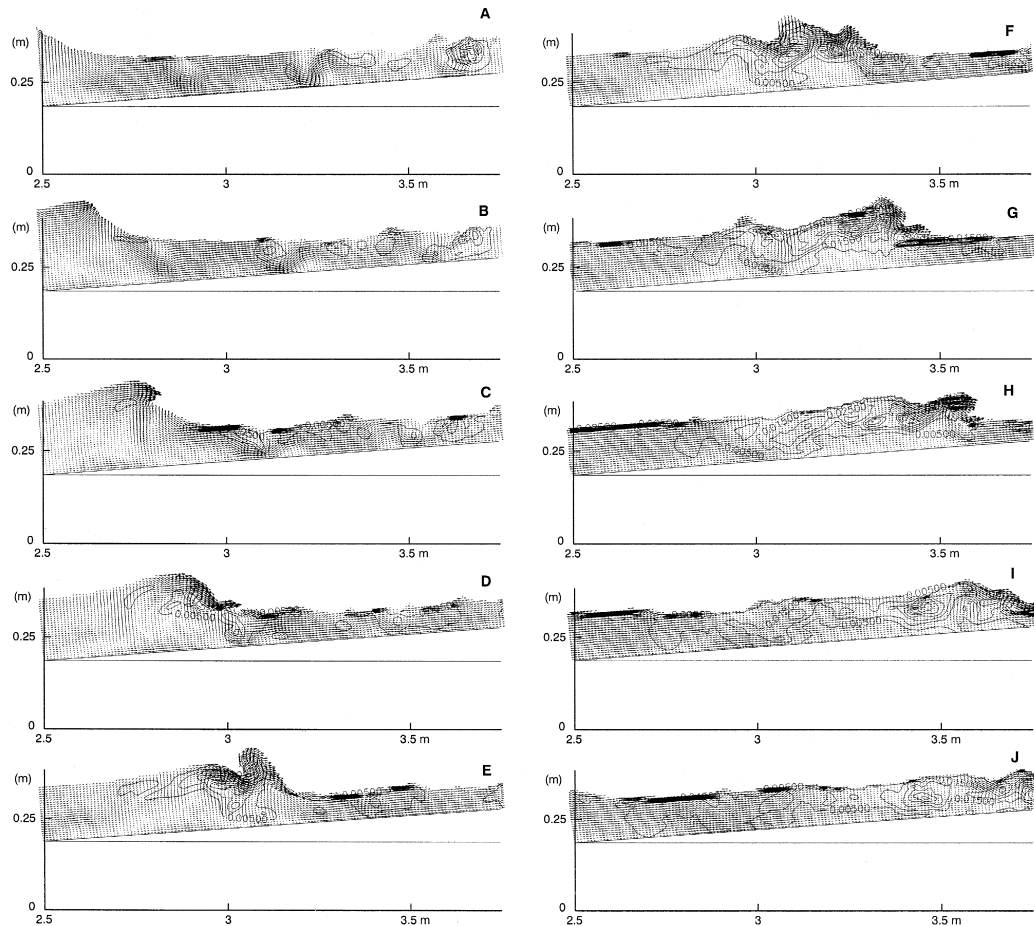


Fig. 15. The time evolution of the turbulent kinetic energy in a weak plunging breaker. Contour lines as in Fig. 13.

ing is used when the waves are generated by a regular periodic motion of the wave generator (or by several repetitions of a short time series). The assumption is that the non-turbulent motion is periodic, and the signal is sampled at regular intervals through the wave period. The measurements taken at the same phase in the wave motion are binned, and the average value over a large number of waves is taken as the ordered wave motion and the deviation from the mean is taken as the turbulent fluctuation. It has been pointed out (Nadaoka et al., 1989) that the turbulence in the surf zone from one breaking wave may affect the exact position of the breaking point of the next, thereby adding a non-deterministic contribution to the velocity signal, even though the forcing from the wave generator is periodic. This non-de-

terministic but ordered velocity contribution can be very large, for example near a shear layer, where the measuring position may be at the high velocity side of the shear layer under some of the waves and on the low velocity side under the rest of the waves.

In the analysis of the present simulations, it has been utilized that the velocities are available simultaneously in the entire computational area. Uniform conditions in the longshore direction have been simulated, and the surface boundary has been treated as being cylindrical with each surface marker acting as a line parallel with the  $y$ -axis. The average of a quantity in the  $y$ -direction can therefore be interpreted as belonging to the ordered motion, and the deviation from the average as the turbulent fluctuation. This analysis has the advantage that a detailed

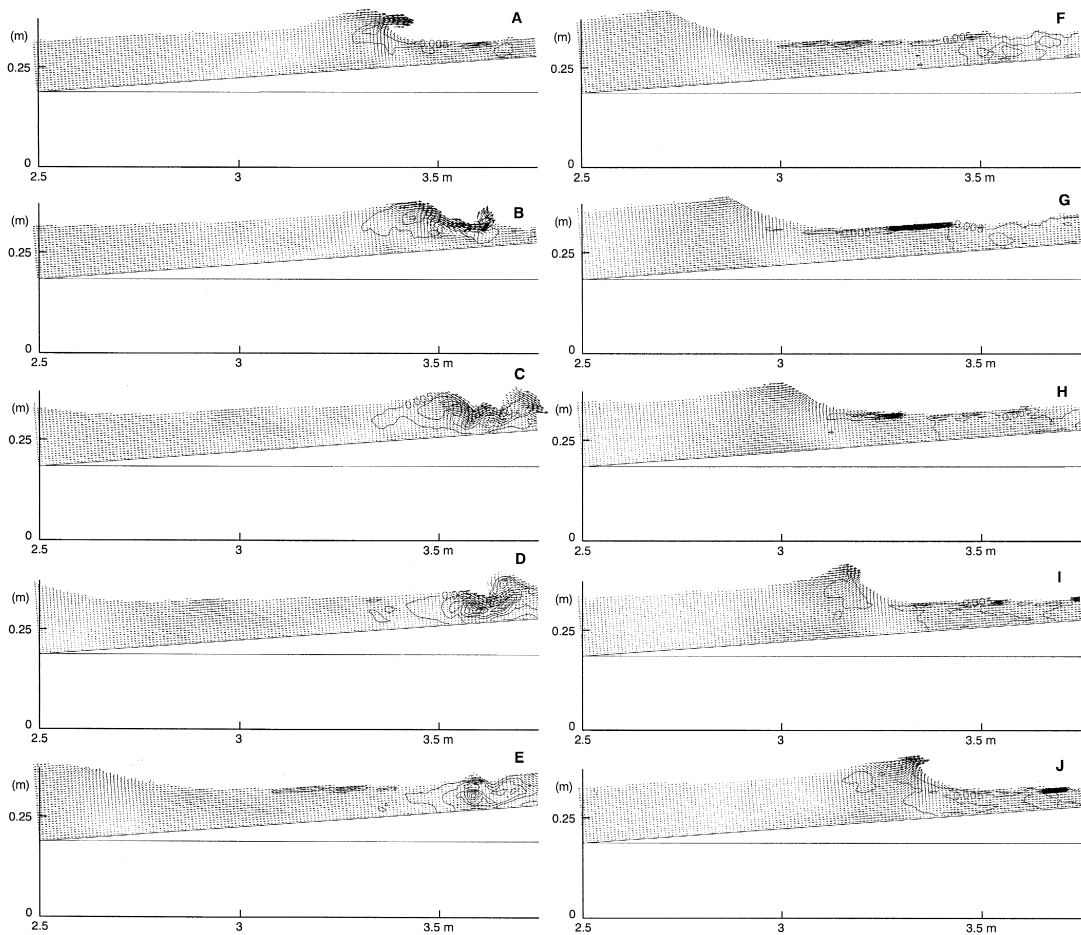


Fig. 16. The time evolution of the turbulent kinetic energy in a strong plunging breaker. Contour lines as in Fig. 13.

spatial distribution of the turbulence can be obtained from a few data sets with the instantaneous velocities from the entire computational area, rather than detailed time series from a large number of data points. The two-dimensionality of the surface can be expected to cause some reduction in the turbulence level close to the surface compared to a situation where a completely three-dimensional representation of the surface is introduced.

The velocity is thus split into a mean quantity  $\bar{u}$ , averaged in the direction parallel to the coastline, and a turbulent fluctuation  $u'$ :

$$u = \bar{u} + u' \quad (14)$$

and the turbulent kinetic energy is defined as:

$$k = \frac{1}{2} (\overline{u'^2} + \overline{v'^2} + \overline{w'^2}) \quad (15)$$

An example of the distribution of the turbulent velocity fluctuations determined by the averaging procedure is shown in Fig. 12. The three velocity components under the weak plunging breaker are shown along a plane parallel with the bed at a distance of 3.3 cm from the bed. The thick solid line represents the velocities averaged in the transverse direction, and the thin broken curves are the velocities distributed along four lines at different positions. It can be seen that the averaged velocities in the  $x$ - and  $z$ -directions contain significant short period oscillations. This may partly reflect that the breaking induces two-dimensional fluctuations with length scales comparable to the most energetic turbulent eddies and partly because the width of the calculation domain is too small to obtain stable statistics.

A comparison of the distributions of the turbulent kinetic energy in a spilling, a weak plunging and a strong plunging breaker is given in Fig. 13. The three waves are shown approximately half a wave period after the initial breaking. The transversely averaged velocity field and the contours of the turbulent energy from the first two small computational blocks are shown. The spilling breaker is characterized by four or five relatively large horizontal eddies. Beneath these eddies, turbulence is produced continuously as the broken wave propagates towards the shoreline. The turbulence is gradually spread over the entire water column by convection and turbulent diffusion. The horizontal extension of the region

with a high intensity of the turbulence is about five times the water depth. The maximum level of the turbulent kinetic energy in the spilling breaker is  $0.05 \text{ m}^2/\text{s}^2$ , corresponding to about  $0.04 \text{ gD}$ . This gives a maximum in the root-mean square value of the turbulent velocity fluctuations of  $0.15\sqrt{gd}$ , which is of the same order of magnitude as found in the experiments of Ting and Kirby (1994, 1996), where the conditions are comparable to the situation considered here.

In the weak plunging breaker, the horizontal eddies are less pronounced than for the spilling breaker. The generation of turbulence is still strongly related

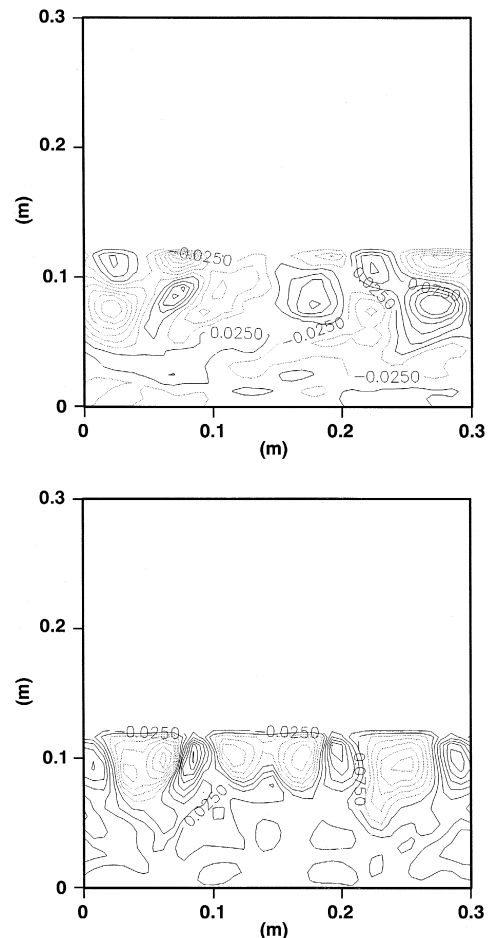


Fig. 17. Contour plots of the  $v$  and  $w$  velocity components in the  $y$ - $z$  plane, weak plunging breaker,  $x = 3.20 \text{ m}$ , half a wave period after the breaking — corresponding to panel H in Fig. 15.

to the propagation of the front of the broken wave. The turbulence spreads faster and reaches the bed earlier in this case. An area with a high intensity in the turbulence is seen about 0.6 m from the left boundary. This maximum is related to the formation of the obliquely descending eddies considered above. The maximum in the turbulence level is similar to the spilling breaker case, but the horizontal extension of the area with a high intensity of the turbulence is smaller.

For the strong plunging breaker, the generation of turbulence is different from the first two cases. Though small horizontal eddies are present, the area of high intensity turbulence is well behind the front, and has been generated at an earlier stage of the breaking. The turbulence is distributed over the whole water column and with two distinct areas of high turbulence intensity.

The temporal development of the breaking process and production and decay of turbulence during a wave period for each of the three cases are illustrated in Figs. 14–16. For the spilling breaker, Fig. 14, the shear region and the surface roller are formed almost immediately after the initial breaking. The shear between the roller and the back-rush beneath it causes a strong instability and the development of a series

of horizontal eddies. The production of turbulence is, as mentioned above, concentrated under these eddies. The highest levels of turbulence are found in Fig. 14E, which is identical to Fig. 13a. The turbulence has not been completely dissipated before the next wave breaks. In this figure and the following two, several spots of turbulence can be observed just at the surface even in regions where the general turbulence level is low. This is not physical, but may be caused by the formulation or the implementation of the free surface which is only two-dimensional.

When the weak plunger breaks, a tongue of water is thrown out in front of the wave. The tongue falls down on the slope in front of the crest. Behind the point of impingement strong vorticity is generated, cf. Fig. 9, but no significant turbulence is generated at this stage. In Fig. 15E, it is seen how the plunging tongue pushed a volume of water up in front of itself and generation of turbulent kinetic energy is initiated. As the broken wave continues toward the shoreline it resplashes several times, and each new splash acts as a source of turbulence. Even though the plunging tongue of water does not penetrate the surface, the horizontal eddies nearly reach the bed, causing the turbulence to be distributed over the entire water column.

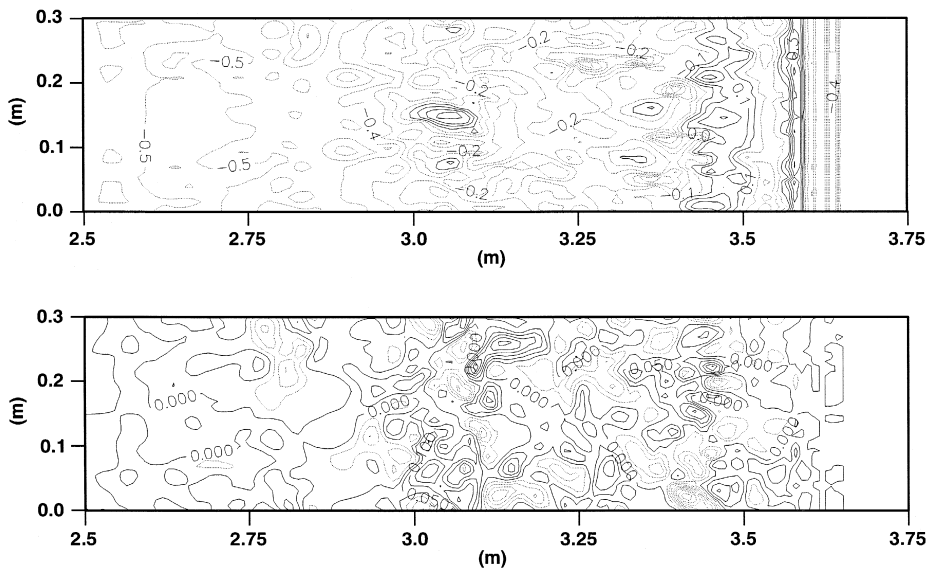


Fig. 18. Contour plots of the  $u$  and  $v$  velocity components in the  $x$ - $y$  plane, weak plunging breaker. 5.7 cm from the bed, half a wave period after the breaking — corresponding to panel H in Fig. 15.

In the first phases of the breaking of the strong plunging breaker, Fig. 16A, a tongue or jet of water is directed in the horizontal direction from the crest of the wave. The tongue plunges in the trough and pushes a mass of water up in front of itself. The initial penetration of the tongue is weak, especially for this particular breaker where the direction of the flow velocities in the tongue is more horizontal than for the previous breakers in the simulation run. It may, however, be noted that immediately after the plunge (Fig. 16C), a significant part of the horizontal momentum of the tongue of water has been transferred to a part of the water column under the plunge

point. Behind the point of impingement strong vorticity is introduced by the initial breaking, which may be interpreted as topologically generated vorticity. The vortices and the turbulent kinetic energy are spread over the entire water column and reach the bed soon after the impingement, Fig. 16C,D. The broken wave resplashes generating strong vorticity, and two distinct regions of turbulence can be observed (cf. Fig. 13c, where the entire calculation domain is depicted at the instant corresponding to Fig. 16E): one related to the initial breaking and one related to the resplashing of the water pushed up by the plunger. The last panels of Fig. 16 show that the

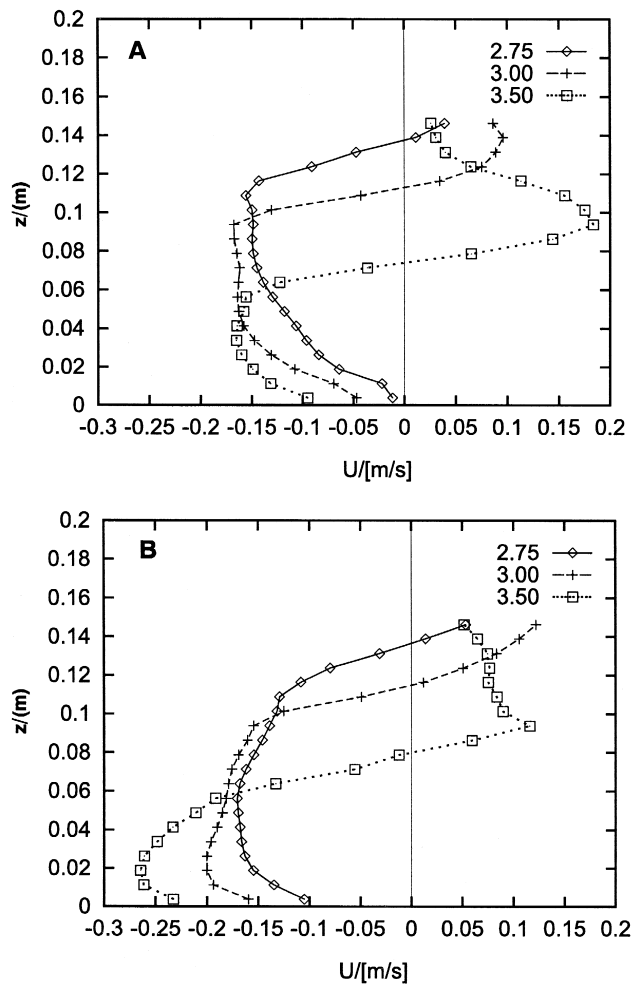


Fig. 19. Mean velocity, averaged over four wave periods, weak plunging breaker at  $x$  equal 2.75 m, 3.00 m and 3.25 m. (A) No-slip condition at the bed. (B) Log law-of-the wall at the bed.

turbulent kinetic energy dissipates rather fast, and the turbulence level is very low when the next wave starts to break.

A turbulence field can be characterized by different length scales. The two most important are the micro length scale or Taylor length scale which characterizes the size of the turbulent eddies that dissipate the turbulent energy into heat and the macro length scale which characterizes the size of the eddies that contain the dominant part of the turbulent energy. The macro length scale can also be used as a measure of the length scale in the turbulent exchange processes through parameters like the eddy viscosity or the turbulent diffusion coefficient. In LESs, the macro length scales may be determined by analysis of the simulation results while the motions on the micro length scale are not resolved by the model.

The macro length scale can be determined as the integral of the auto-correlation in space, but in the present simulations the extension of the model domain in the transverse direction was found to be too small to give a proper resolution of the auto-correla-

tion function (or a wave number spectrum). Use of ensemble averaging could give the necessary number of independent determinations of auto-correlations, but with the difficulties of making ensemble averaging in the present numerical experiments described earlier and the very few wave periods that could be simulated, this approach was not possible either. The length scale has therefore been estimated from a visual inspection of the velocity fields, simply counting the number of zero-crossings for a velocity component across the computational domain. A few examples of the results obtained by this rather crude method are presented.

Fig. 17 shows contour plots of the velocity components in a cross-section in the  $y$ - $z$  plane of the weak plunging breaker. The cross-section is at  $x$  equal 3.20 m and approximately half a wave period after the initial breaking, corresponding to Fig. 15H. The  $v$  and the  $w$  components of the velocities change sign about six times across the width of the cross-section corresponding to a wavelength scale of the fluctuations of about  $1/3$  of the width of the compu-

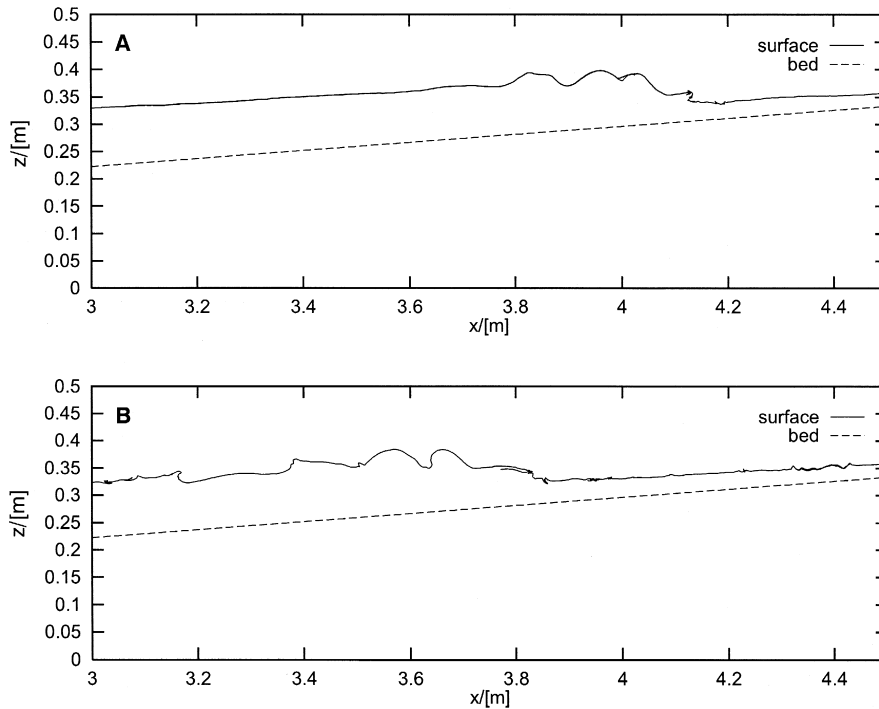


Fig. 20. The position of the surface after simulation of four wave periods. (A) No-slip condition at the bed. (B) Log law-of-the wall at the bed.

tational domain, which is 30 cm. The contour plots in Fig. 18 illustrate the  $u$  and  $v$  components in a plane parallel with the bed and 5.7 cm above it. The length scale here is found to be in the range from 1/5 to 1/3 of the width of the computational domain or of the order one half of the water depth.

Similar plots have been analysed for the spilling breaker and for the strong plunging breaker. The length scales in the transverse direction are still found typically to be in the range 1/3 to 1/5 of the width of the domain.

In the weak plunger case, it was investigated if the characteristic wavelength scales were changed in a simulation with a doubled width of the domain. This was not found to be the case which indicates that a width of the domain of 30 cm is just large enough to simulate the relevant scales of the large eddies in the turbulence.

#### 5.4. Sensitivity to the boundary conditions

The sensitivity of the calculations to modifications in the boundary conditions has been investigated by a series of simulations of the weak plunging breaker with slightly coarser grids than used in the previous simulations. Periodic boundary conditions has been used on the lateral boundaries to have best agreement with the assumption of an infinitely long beach. In order to check that the width of the domain is large enough, a slip boundary condition with no flux has also been applied. No significant difference has been found between the main results obtained by the two boundary conditions. Two different bed boundary conditions have been compared: a no-slip condition and the wall law based on a logarithmic velocity profile described above. Fig. 19 illustrates the mean velocity profiles obtained by using the two boundary conditions. The mean velocity profiles are clearly different. The log-law condition gives a stronger mean undertow current and larger near bed velocities. Comparison with mean velocity profiles from experiments (Ting and Kirby, 1994) clearly indicates that the results obtained by the log-law are more realistic than the no-slip boundary condition. Fig. 20 shows the position of the free surface at the same time in the simulation (after four wave periods) for the two bed boundary conditions. The differences are significant: particularly it can be seen how the

weaker undertow and backrush with the no-slip boundary condition allows the front of the breaking wave to advance faster than the stronger undertow in the case of a log-law bed boundary condition.

## 6. Conclusions

A three-dimensional hydrodynamic model has been combined with a free surface model to simulate the flow field in breaking waves. The large turbulent eddies containing most of the turbulent energy have been simulated by the LES method where the small scale turbulence, which is not resolved by the hydro-

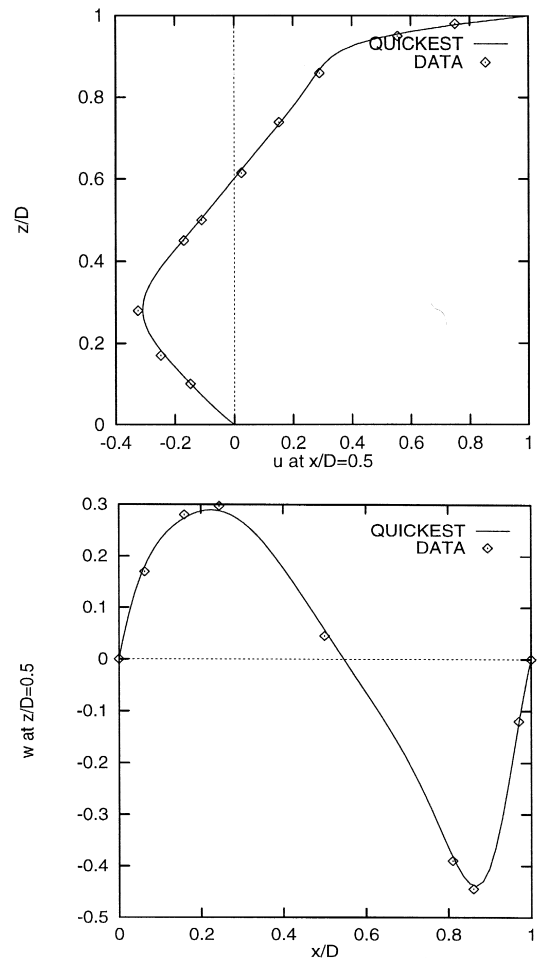


Fig. A1. The velocity profiles in the two-dimensional driven cavity. Reynolds number:  $Re = 400$ .

dynamic simulation, is represented by a simple Smagorinsky sub-scale model.

The free surface is described by the surface marker method. A full representation of the three-dimensional water surface would require an excessively high number of surface markers and a correspondingly high computational effort. Instead, the free surface is represented by a single cross-shore profile of surface markers and assuming that the surface is uniform in the longshore direction and moving according to the cross-shore average of the surface velocities. It was found that full three-dimensional turbulence field develops readily after the wave breaking when the three-dimensional flow model is applied in combination with the two-dimensional water surface. The free surface boundary causes an introduction of additional water in the model particularly when the breaking wave turns over. This (combined with the requirement of prohibitively large computational resources) precludes simulation of a large number of wave periods and averaging over several waves.

The turbulence can be distinguished from the mean motion by making an average across the modelling domain (in the direction of the wavefronts). Three cases have been considered, spilling breakers and weak and strong plunging breakers. The mean motion and the turbulent kinetic energy have been analysed in the three cases. Although the conditions in the simulations are not identical to experiments where turbulence has been measured, the order of

magnitude of the turbulent energy is found to be in agreement with experimental results. There is a marked difference in the flow field under the different types of breakers.

Under the spilling breaker a roller is formed with a shear layer beneath it. Behind the front of the breaking/broken wave a series of eddies are formed. The turbulence is produced in the shear layer and the eddies, and is gradually decaying spreading down towards the bed after the passage of the front.

In the strong plunging breaker, a strong localized production of turbulence takes place at the plunge point in connection with the topologically generated vorticity. The turbulence is spread over the vertical almost immediately due to the large, mainly two-dimensional vortices that extend over the entire water depth. The production of turbulence is repeated further inshore when the amount of water that is pushed up plunging jet resplashes, and two distinct zones of turbulence can be observed. The weak plunger causes a turbulence pattern in between those of the spilling and the strong plunging breaker.

Distinct three-dimensional eddies were often generated behind the two-dimensional vortices following the front of the wave. In some instances, they extended all the way to the bed and could be interpreted as obliquely descending eddies.

The length scale of the turbulence that is resolved by the model has been estimated by visual inspection. For a spilling breaker, the two-dimensional horizontal eddies had a typical length scale of  $1/3$  of

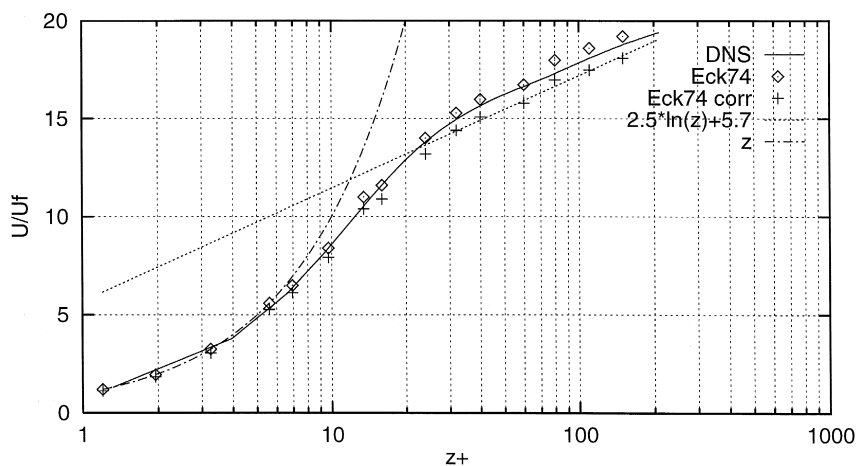


Fig. A2. Mean velocity profile compared to measurements by Eckelmann (1974) and corrections presented by Kim et al. (1987).

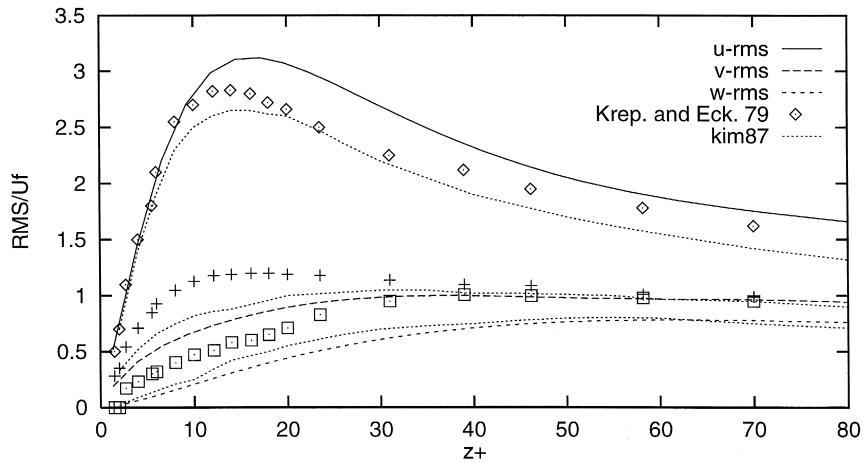


Fig. A3. Root-Mean-Square of the velocity fluctuations:  $\sqrt{\overline{u'^2}}/U_f$ ,  $\sqrt{\overline{v'^2}}/U_f$ ,  $\sqrt{\overline{w'^2}}/U_f$ , as functions of the distance from the bed in wall units,  $U_f$  is the friction velocity, the Reynolds number is  $Re = 3500$ .

the water depth. For a plunging breaker, they can extend over the entire water column. The length scale of the transverse turbulent fluctuations were typically of the order one half of the water depth.

Research and Development, in the SASME project under contract No. MAS3 CT97-0081 and by the Danish Technical Research Council under the frame programme: 'Kyster og tidevandsløb'.

## Acknowledgements

The authors are indebted to Prof. Jørgen Fredsøe for inspiration and suggestions during the work. This work has been supported by the Commission of the European Union, Directorate General for Science,

## Appendix A. Verification of numerical models

This appendix shows a basic verification of the code. The verification is made by comparison of some canonical flow cases testing each part of the produced code to a satisfactory level.

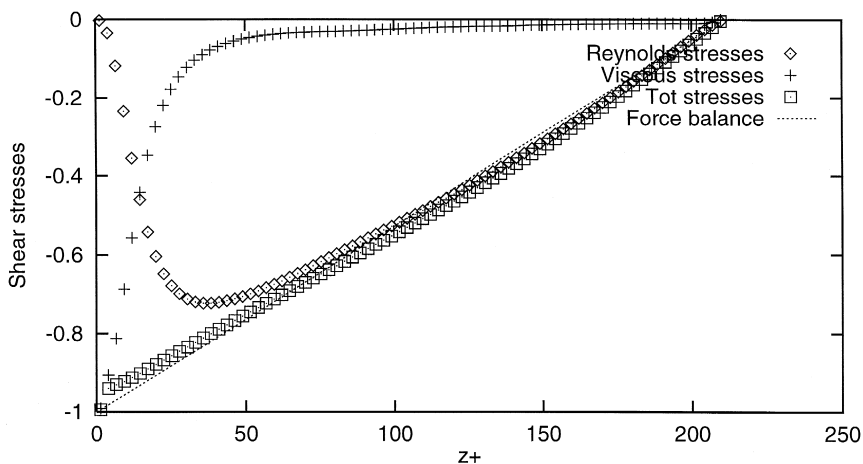


Fig. A4. The vertical distribution of the contributions to the mean shear stress, normalized by the wall shear stress.

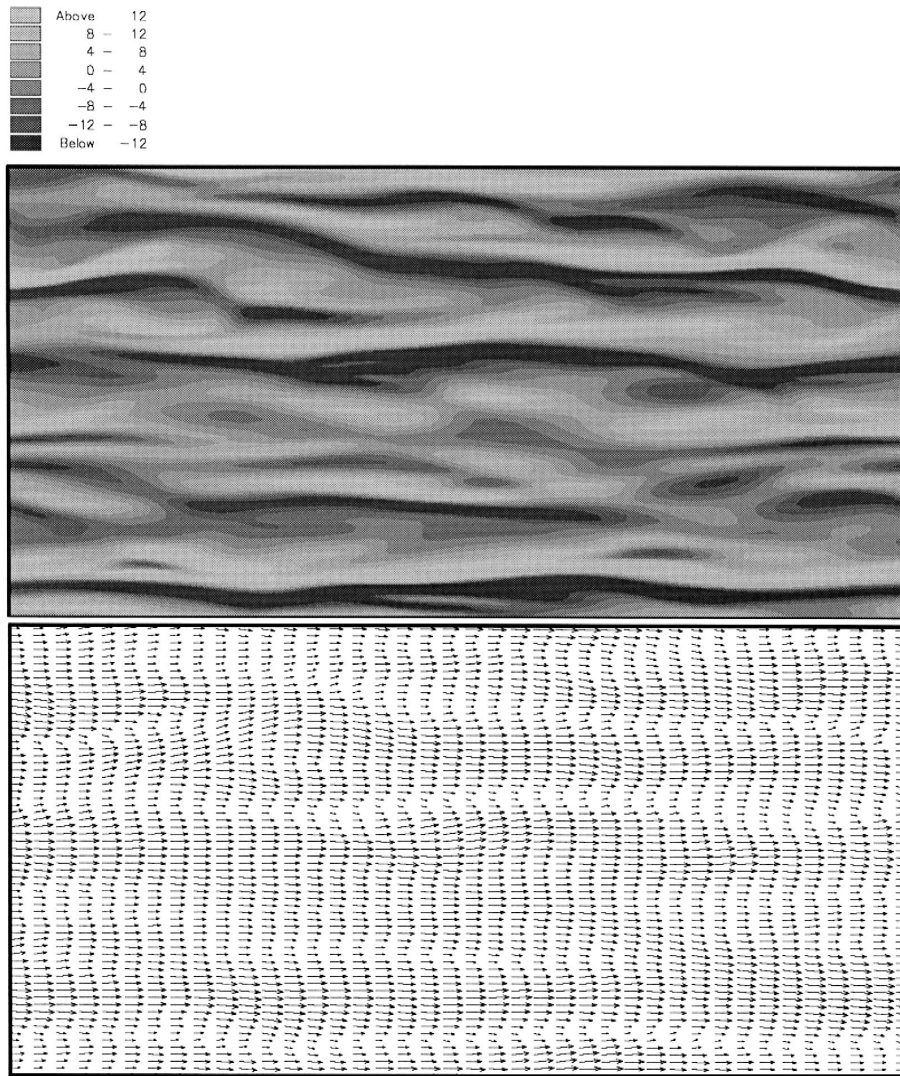


Fig. A5. A vorticity plot and vector plot of the velocity field 12 wall unit from the bed.

### A.1. The Navier–Stokes solver

Two tests show the capability of solving the Navier–Stokes equations. The first is a driven cavity problem in two-dimensions and the second a Direct Numerical Simulation of a channel flow.

Fig. A1 shows an example of the cavity problem for a Reynolds number of 400. The Reynolds number is based on the velocity of the driven lid, the depth of the cavity and the viscosity:  $Re = U_{\text{lid}} D / \nu$ . The grid consists of  $64 \times 64$  cells of identical size. After stationary conditions have been achieved the

cross-sectional velocity profiles are extracted and compared to measurements (Ghia et al., 1982).

The next figures show the results from a direct numerical simulation (DNS) of a turbulent open channel flow. The upper boundary is treated as an impermeable slip surface, which will have only very small effect on the near bottom turbulence that is the main interest of the simulation. The length scale is made dimensionless as:

$$z^+ = U_f \frac{z}{\nu} \quad (\text{A1})$$

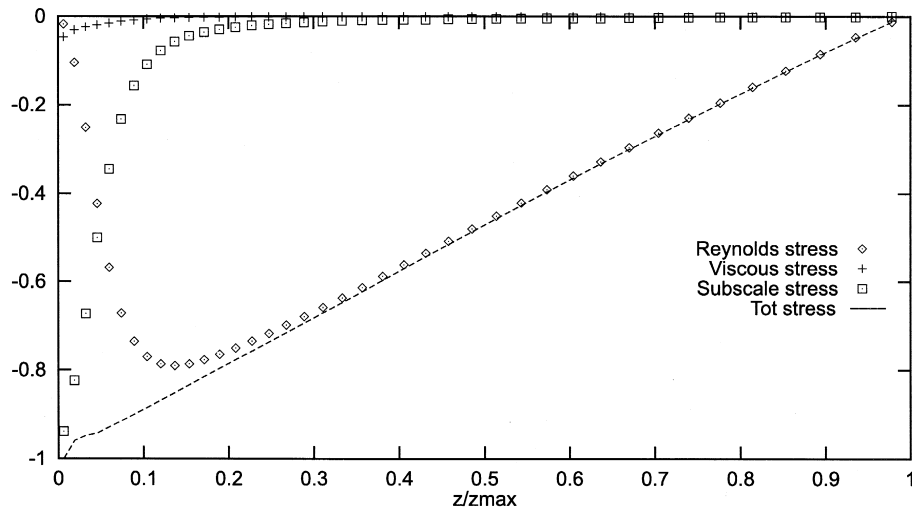


Fig. A6. The contributions to the time-averaged shear stress distribution, Large Eddy Simulation, bed roughness: 2 mm, Reynolds number:  $Re = 100,000$ .

where  $U_f$  is the friction velocity and  $\nu$  the kinematic viscosity. The friction velocity is found from the force balance. The length found from Eq. (A1) is referred to as wall units. The computational domain is 1266 wall units long, 633 wide and 211 deep and consists of  $80 \times 128 \times 80$  cells. The Reynolds number is 3500 and the numerical experiment is comparable to Kim et al. (1987). The Reynolds number is

based on the average velocity, the depth of the channel and the kinematic viscosity.

Fig. A2 shows a comparison to the experiments by Eckelmann (1974) and to the DNS by Kim et al. (1987). The RMS-values of the fluctuating part of the velocity divided by the friction velocity is shown in Fig. A3. The results are compared to the experiments by Kreplin and Eckelmann (1979) and to the

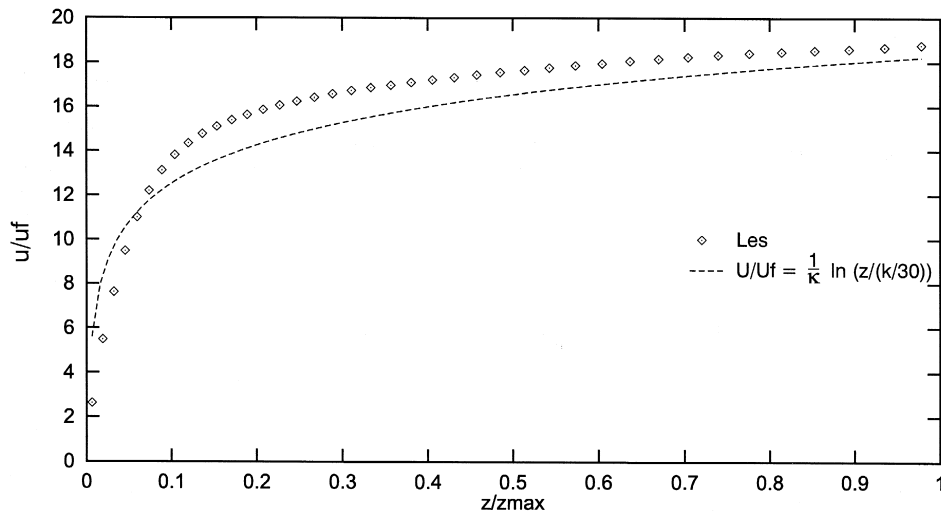


Fig. A7. Comparison between the mean velocity profile simulated by LES and a logarithmic velocity profile, bed roughness: 2 mm, Reynolds number:  $Re = 100,000$ .

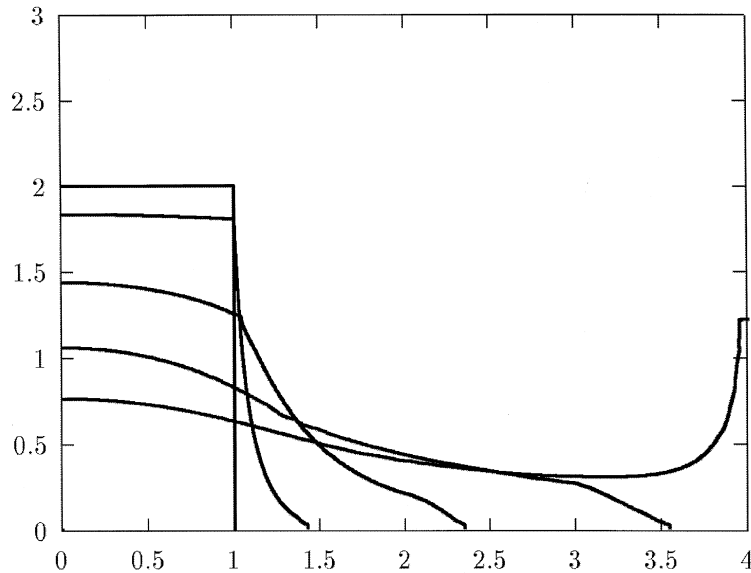


Fig. A8. The profiles of the free surface in a dam-break at five values of the dimensionless time:  $t^* = 0.0, 0.88, 1.77, 2.65$  and  $3.54$ .

DNS by Kim et al. (1987). A time averaged force balance is given in Fig. A4, which shows the variation over the vertical of the Reynolds shear stress, the mean viscous shear stress, the sum of the two (total) and the linear distribution of the mean shear stress determined from a force balance between the

shear stress and the driving force (pressure gradient). The agreement with earlier work is found to be satisfactory and shows that the code is capable of simulating the turbulent processes.

Low speed streaks is a common feature of near wall turbulence over a smooth boundary and an

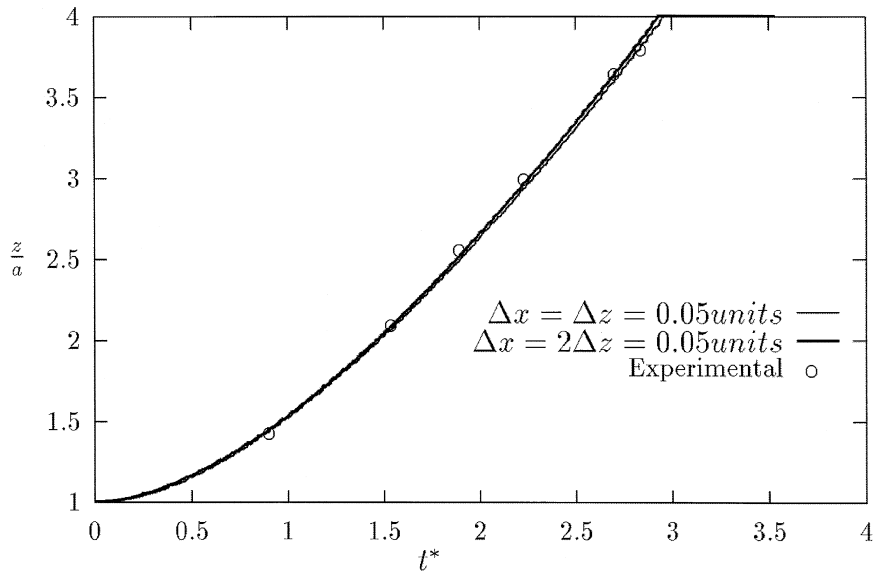


Fig. A9. Comparison of the calculated position of the toe of the emerging dam-break with experimental data from Martin and Moyce (1952).

example of the low speed streaks is shown in Fig. A5. The figure shows the vorticity and the velocity vectors in a plane 12 wall units above the bed. Five to seven streaks are observed across the flow domain. The width of the cross-section is 633 wall units giving a spacing between the streaks around 100 wall units.

### A.2. The Subgrid Scale model

A LES of a channel flow with an impermeable slip lid has been made. To be consistent with the surf zone model, which is the main tool in this study, the simple Smagorinsky (1963) closure model has been applied. The simulation is thus less advanced than the present state-of-the-art for LES simulations of, e.g. channel flows and on a level comparable to the work of Schumann (1975). The subgrid model is included to be able to simulate flows at high Reynolds numbers and as an example of a high Reynolds number flow an open channel flow is simulated. The Reynolds number based on the average velocity, the depth of the channel and the kinematic viscosity is 100,000, and the wall roughness divided by the depth is,  $k/D = 50$ , corresponding to a depth of 0.1

m and a roughness of 2 mm. The domain consists of  $80 \times 64 \times 40$  cells with a weak stretching of the grid near the bed. At the top boundary slip conditions are applied, while wall functions based on a logarithmic law of the wall are used near the bed (cf. Christensen, 1998). The averaged velocity profile and the force balance are shown in Figs. A6 and A7. The force balance in Fig. A6 illustrates the vertical distribution of the three contributions to the mean shear stress: the Reynolds shear stress resolved by the model, the mean viscous shear stress and the mean shear stress of the model for the unresolved subgrid turbulence. The total of the three contributions is seen to be close to the linear distribution determined by a total force balance. The sub grid turbulence dominates very close to the bed, while the viscous contribution is less significant because of the simulation of the rough bed with a wall function.

### A.3. The free surface model

One of the most common cases used for validation of free surface methods has been the two-dimensional dam-break problem. The fluid is at the initial stage placed in a column that is two units high and

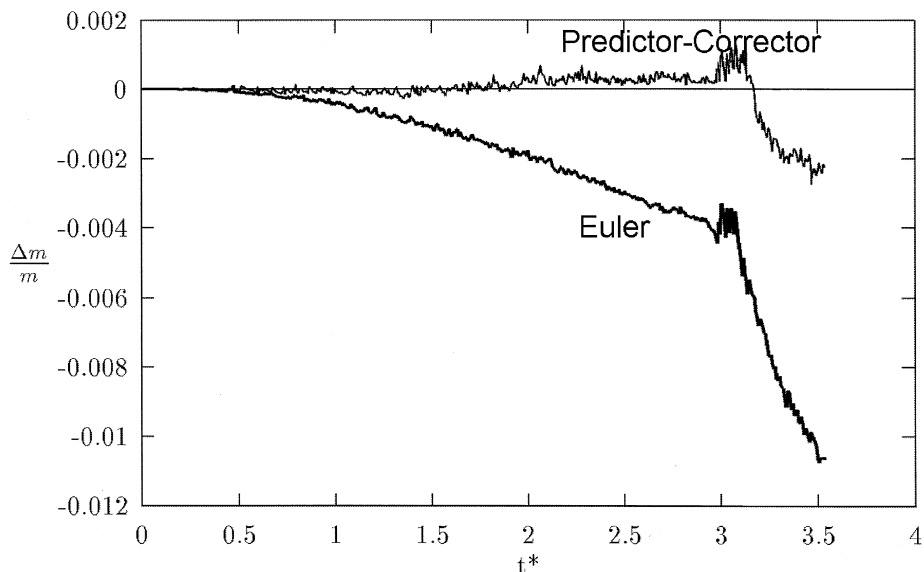


Fig. A10. The relative loss/gain of water during the dam-break for the two different methods of calculating the marker positions: the plain Euler method and the Predictor–Corrector method. With both methods, an increase in the mass deficit occurs as the advancing toe of water hits the wall to the right of the water column.

one unit wide. The quantities are made dimensionless by the width of the column of water,  $a$ , and time is made dimensionless by  $\sqrt{a/g}$ , where  $g$  is the gravitational acceleration. The viscosity is set to a very low value and slip conditions are applied on all boundaries. The computational domain is  $4a$  long and  $3a$  high. There are 80 cells in the horizontal direction and 60 in the vertical.

Fig. A8 shows an example of the dam-break simulation. Fig. A9 shows the distance travelled by the toe of the fluid expanding to the right as a function of time. A comparison is made to the experiments in Martin and Moyce (1952). The gain/loss of mass  $\Delta m$  in the computational domain is illustrated in Fig. A10 for the two methods used to calculate the surface marker positions. The Predictor–Corrector method is seen to conserve mass to a higher degree of accuracy.

## References

- Basco, D.R., 1985. Qualitative description of wave breaking. *J. Waterways Port, Coast. Ocean Eng.* ASCE 3 (2), 170–188.
- Battjes, J.A., 1988. Surf-zone dynamics. *Annu. Rev. Fluid Mech.* 20, 257–293.
- Battjes, J.A., 1974. Computation of set-up, longshore currents, run-up and overtopping due to wind-generated waves, Delft University of Technology, Communications on Hydraulics, 74-2.
- Chen, S., Johnson, D.B., Raad, P.E., 1991. The surface marker method. *Computational Modelling of Free and Moving Boundary Problems*, vol. 1, pp. 226–234, Fluid Flow, de Gruyter, New York.
- Chen, S., Johnson, D.B., Raad, P.E., 1995. Velocity boundary conditions for the simulation of free surface flows. *J. Comput. Phys.* 116, 262–276.
- Christensen, E.D., 1998. Large eddy structures under breaking waves, Series Paper 67, Dept. Hydrodynamics and Water Resources (ISVA), Technical University of Denmark, 140 pp.
- Deigaard, R., Fredsøe, J., Hedegaard, I.B., 1986. Suspended sediment in the surf zone. *J. Waterways Port, Coast. Ocean Eng.*, ASCE 112 (1), 115–128.
- Eckelmann, H., 1974. The structure of the viscous sublayer and the adjacent wall region in a turbulent channel flow. *J. Fluid Mech.* 65, 439–459.
- Fenton, J.D., 1972. A ninth order solution for the solitary wave. *J. Fluid Mech.* 53 (2), 257–271.
- Ferziger, J.H., Peric, M., 1999. *Computational methods for fluid dynamics*. 2nd. edn. Springer, Berlin, 389 pp.
- Galperin, B., Orszag, S.A., 1993. *Large Eddy Simulation of Complex Engineering and Geophysical Flows*. Cambridge Univ. Press.
- Galvin, C.J., 1968. Breaker type classification on three laboratory beaches. *J. Geophys. Res.* 73 (12), 3651–3659.
- George, R., Flick, R.E., Guza, R.T., 1994. Observations of turbulence in the surf zone. *J. Geophys. Res.* 99 (C1), 801–810.
- Germano, M., Piomelli, U., Moin, P., Cabot, W.H., 1991. A dynamic subgrid-scale eddy viscosity model. *Phys. Fluids A* 3 (7), 1760–1765.
- Germano, M., 1992. Turbulence: the filtering approach. *J. Fluid Mech.* 238, 325–336.
- Ghia, I., Ghia, K.N., Shin, C.T., 1982. High-Re solutions for incompressible flow using the Navier–Stokes equations and a multigrid method. *J. Comput. Phys.* 48, 387.
- Grilli, S.T., Subramanya, R., Svendsen, I.A., Veeramony, J., 1994. Shoaling of solitary waves on plane beaches. *J. Waterways Port, Coast. Ocean Eng.* ASCE 120 (6), 609–628.
- Jansen, P., 1986. Laboratory observations of the kinematics in the aerated region of breaking waves. *Coast. Eng.* 9, 453–477.
- Kawamura, T., Mayer, S., Garapon, A. and Sørensen, L., 2000. Large Eddy Simulation of flow past a surface piercing circular cylinder, *J. Fluid Mechanics*, submitted.
- Kim, J., Moin, P., Moser, R., 1987. Turbulence statistics in fully developed channel flow at low Reynolds number. *J. Fluid Mech.* 177, 133–166.
- Kreplin, H., Eckelman, H., 1979. Behavior of the three fluctuating velocity components in the wall region of turbulent channel flow. *Phys. Fluids* 22, 1233–1239.
- Lemos, C.M., 1992. Wave Breaking. A numerical study. *Lecture Notes in Engineering*, vol. 71, Springer-Verlag.
- Leonard, A., 1974. On the energy cascade in large-eddy simulations of turbulent fluid flows. *Adv. Geophys.* 18A, 237–248.
- Leonard, B.P., 1979. A stable and accurate convective modelling procedure based on quadratic upstream interpolation. *Comput. Meth. Appl. Mech. Eng.* 19, 59–98.
- Lin, C., Hwung, H.H., 1992. External and internal flow fields of plunging breakers. *Exp. Phys.* 12, 229–237.
- Lin, P., Liu, P.L.F., 1998a. Turbulence transport, vorticity dynamics, and solute mixing under plunging breaking waves in surf zone. *J. Geophys. Res.* 103 (C8), 15677–15694.
- Lin, P., Liu, P.L.F., 1998b. A numerical study of breaking waves in the surf zone. *J. Fluid Mech.* 359, 239–264.
- Madsen, P.A., Sørensen, O.R., Schäffer, H.A., 1997a. Surf zone dynamics simulated by a Boussinesq type model. Part I. Model description and cross-shore motion of regular waves. *Coast. Eng.* 32 (4), 255–287.
- Madsen, P.A., Sørensen, O.R., Schäffer, H.A., 1997b. Surf zone dynamics simulated by a Boussinesq type model. Part II: Surf beat and swash oscillations for wave groups and irregular waves. *Coast. Eng.* 32 (4), 289–319.
- Martin, J.C., Moyce, W.J., 1952. An experimental study of the collapse of liquid columns on a rigid horizontal plane. *Philos. Trans. R. Soc. London, Ser. A* 244, 312.
- Mason, P.J., Callen, N.S., 1986. On the magnitude of the subgrid-scale eddy coefficient in large-eddy simulations of channel flow. *J. Fluid Mech.* 162, 439–462.
- Mayer, S., Garapon, A., Sørensen, L., 1998. A fractional step method for unsteady free surface flow with application to non-linear wave dynamics. *Int. J. Numerical Meth. Fluids* 28, 293–315.

- Miyata, H., 1986. Finite-difference simulation of breaking waves. *J. Comput. Phys.* 65, 179–214.
- Nadaoka, K., Hino, M., Koyano, Y., 1989. Structure of the turbulent flow field under breaking waves in the surf zone. *J. Fluid Mech.* 204, 359–387.
- Nadaoka, K., Kondoh, T., 1982. Laboratory measurements of velocity field structure in the surf zone by LDV. *Coast. Eng. Jpn.* 25, 125–145.
- Nadaoka, K., Ueno, S., Igarashi, T., 1988. Sediment suspension due to large scale eddies in the surf zone. *Proc. 21st Int. Coastal Eng. Conf., Malaga, ASCE*, vol. 2, pp. 1647–1660.
- Nichols, B.D., Hirt, C.W., Hotshkiss, R.S., 1980. SOLA-VOF: A numerical algorithm for transient fluid flow with multiple free boundaries, Technical Report LA-8355, Los Alamos Scientific Laboratory, 107 pp.
- Okayasu, A., Shibayama, T., Horikawa, K., 1988. Vertical variation of undertow in the surf zone. *Proc. 21st Coastal Eng. Conf., Costa del Sol, Malaga, Spain*. pp. 478–491.
- Pedersen, C., Deigaard, R., Fredsøe, J., Hansen, E.A., 1995. Simulation of sand in plunging breakers. *J. Waterways Port, Coast. Ocean Eng. ASCE* 121 (2), 77–87.
- Peregrine, D.H., 1983. Breaking waves on beaches. *Annu. Rev. Fluid Mech.* 15, 149–178.
- Rakha, K.A., Deigaard, R., Brøker, I., 1997. A phase-resolving cross shore sediment transport model for beach profile evolution. *Coast. Eng.* 31, 231–261.
- Sakai, T., Mizutani, T., Tanaka, H., Tada, Y., 1986. Vortex formulation in plunging breakers. *Proc. 20th Int. Conf. Coastal Eng., ASCE, Taipei, Taiwan*, vol. 1, pp. 711–723.
- Schäffer, H.A., Madsen, P.A., Deigaard, R., 1993. A Boussinesq model for waves breaking in shallow water. *Coast. Eng.* 20, 185–202.
- Schumann, U., 1975. Subgrid scale model for finite difference simulations of turbulent flows in plane channels and annuli. *J. Comput. Phys.* 18, 376–404.
- Smagorinsky, J., 1963. General circulation experiments with primitive equations: 1 The basic experiment. *Mon. Weather Rev.* 91, 99–164.
- Stive, M.J.F., 1980. Velocity and pressure field of spilling breakers. *Proc. 17th Coastal Eng. Conf., Sydney*. pp. 547–566.
- Svendsen, I.A., 1987. Analysis of surf zone turbulence. *J. Geophys. Res.* 92 (C5), 5115–5124.
- Ting, F.C.K., Kirby, J.T., 1994. Observations of undertow and turbulence in a laboratory surf zone. *Coast. Eng.* 24, 51–80.
- Ting, F.C.K., Kirby, J.T., 1995. Dynamics of surf zone turbulence in a strong plunging breaker. *Coast. Eng.* 24, 177–204.
- Ting, F.C.K., Kirby, J.T., 1996. Dynamics of surf-zone turbulence in a spilling breaker. *Coast. Eng.* 27, 131–160.
- Zhao, Q., Tanimoto, K., 1998. Numerical simulation of breaking waves by Large Eddy Simulation and VOF method. *Proc. 26th Int. Conf. on Coastal Engineering, ASCE, Copenhagen*, vol. 1, pp. 892–905.